Research Square

Preprints are preliminary reports that have not undergone peer review.
They should not be considered conclusive, used to inform clinical practice,
or referenced by the media as validated information.

XCR1+ and CD11b+ migratory dendritic cells cooperate for the cross-priming of intratumoral CD8+ T cells with a tissue-resident memory phenotype.

Pierre Guermonprez

pierre.guermonprez@pasteur.fr

Institut Pasteur https://orcid.org/0000-0001-5621-2262

Nathan Vaudiau

Institut Pasteur, "Dendritic cells and adaptive immunity" Unit, Immunology Department
https://orcid.org/0000-0001-9586-8467

Pierre Bourdely

Centre de Recherche sur l'Inflammation https://orcid.org/0000-0002-4162-1490

Agathe Ok

Centre de Recherche sur l'Inflammation https://orcid.org/0009-0005-9883-5288

Maria Semitekolou

Institut Pasteur, “Dendritic cells and adaptive immunity” Unit, Immunology Department

Louise Gorline

Institut Pasteur, https://orcid.org/0009-0008-8499-9603

Roberto Savoldelli

King's College London and The Foundation for Liver Research https://orcid.org/0000-0002-4524-9243

Yohan Gerber-Ferder

Institut Cochin, INSERM U1016, CNRS UMR 8104 https://orcid.org/0000-0001-9973-2196

Fillipe Do Carmo

Institut Pasteur, "Dendritic cells and adaptive immunity" Unit, Immunology Department

Aurélie Sémervil

Institut Pasteur, “Dendritic cells and adaptive immunity” Unit, Immunology Department

Mathias Vetillard

Centre de Recherche sur l'Inflammation, INSERM UMR1149

Audrey Rood

Centre de Recherche sur l'Inflammation, INSERM UMR1149

Syrine Bouallègue

Institut Pasteur, “Dendritic cells and adaptive immunity” Unit, Immunology Department

Konstantina Pamboukas

Institut Pasteur,

Jérémie Bornères
Institut Pasteur

Guillaume Darrasse-Jeze
Medicine Faculty of Paris University - INSERM https://orcid.org/0000-0003-3069-8211

Emmanuel Gautier
Inserm UMRS 1269 Nutriomics https://orcid.org/0000-0003-2976-7566

Marc Dalod
CIML Immuology Marseille https://orcid.org/0000-0002-6436-7966

Eric TARTOUR
Department of Immunology, Hôpital Européen Georges Pompidou, AP-HP, Paris
https://orcid.org/0000-0002-7323-468X

Tessa Bergsbaken
Center for Immunity and Inflammation, Department of Pathology, Immunology, and Laboratory Medicine, New Jersey Medical School, Rutgers-the State University of New Jersey
https://orcid.org/0000-0001-8841-8185

Klaas van Gisbergen
Sanquin Research and Landsteiner Laboratory https://orcid.org/0000-0003-3623-7555

Kairbaan Hodivala-Dilke
Barts Cancer Institute, Queen Mary University of London https://orcid.org/0000-0002-2859-749X

Loredana Saveanu
INSERM-UMR1149, Centre de Recherche sur l'Inflammation, Paris https://orcid.org/0000-0003-3138-7968

Julie Helft
Institut Curie https://orcid.org/0000-0002-2733-1972

Federica Benvenuti
International Centre for Genetic Engineering and Biotechnology https://orcid.org/0000-0002-1908-8052

Aboubacar Coulibaly
Institut Pasteur, “Dendritic cells and adaptive immunity” Unit, Immunology Department

Matthieu Rastello
Institut Pasteur, “Dendritic cells and adaptive immunity” Unit, Immunology Department

Marie Guillin
Institut Cochin https://orcid.org/0009-0007-6344-5030

Judith Weber
Institut Cochin https://orcid.org/0009-0001-5349-162X

Abdenour Abbas
Institut Pasteur, "Dendritic cells and adaptive immunity" Unit, Immunology Department
https://orcid.org/0000-0003-2372-4530

Zacarias Garcia
Institut Pasteur
Florent Ginhoux
Singapore Immunology Network (SIgN), A*STAR, Biopolis, Singapore https://orcid.org/0000-0002-2857-7755
Camille Bleriot
Institut Gustave Roussy
Philippe Bousso
Institut Pasteur
Yosuke Kumamoto
Rutgers New Jersey Medical School https://orcid.org/0000-0001-9369-4934
Massimiliano Mazzone
KU Leuven/VIB https://orcid.org/0000-0001-8824-4015

Article

Keywords:

Posted Date: April 9th, 2026

DOI: https://doi.org/10.21203/rs.3.rs-6017264/v1

License: This work is licensed under a Creative Commons Attribution 4.0 International License.
Read Full License

Additional Declarations: There is **NO** Competing Interest.

Version of Record: A version of this preprint was published at Nature Communications on September 18th, 2026. See the published version at https://doi.org/10.1038/s41467-026-77641-7.

XCR1^{+} and CD11b^{+} migratory dendritic cells cooperate for the cross-priming of intratumoral CD8^{+} T cells with a tissue-resident memory phenotype.

Nathan Vaudiau[1,2,3*], Pierre Bourdely[4,5,6,7*], Maria Semitekolou[1,2,3], Agathe Ok[3,4], Louise Gorline[1,2,3], Aboubacar Coulibaly[1,2,3], Matthieu Rastello[1,2,3], Aurélie Semervil[1,2,3,4], Roberto Savoldelli[8], Yohan Gerber-Ferder[5], Fillipe Luiz Rosa do Carmo[1,2,3], Mathias Vétillard[1,2,3], Audrey Rood[4], Jérémie Bornères[1,2,3], Abdenour Abbas[1,2,3], Marie Guillin[5], Judith Weber[5], Syrine Bouallegue[1,2,3], Konstantina Pamboukas[1,2,3], Zacarias Garcia[9], Florent Ginhoux[10,11], Camille Bleriot[10], Philippe Bousso[9], Yosuke Kumamoto[12,13], Guillaume Darrasse-Jèze[14,15] Emmanuel L Gautier[16], Marc Dalod[17], Eric Tartour[18], Tessa Bergsbaken[19], Klaas P J M Van Gisbergen[20], Kairbaan M Hodivala-Dilke[21], Massimiliano Mazzone[6,7], Loredana Saveanu[4], Julie Helft[5], Federica Benvenuti[22], Pierre Guermonprez[1,2,3,§]

[1]Institut Pasteur, “Dendritic cells and adaptive immunity” Unit, Immunology Department, Paris, France.

[2]CNRS UMR3738 “Developmental biology and stem cells”, Institut Pasteur.

[3]Center for Vaccine and Immunotherapy, Institut Pasteur.

[4]Centre de Recherche sur l'Inflammation, INSERM UMR1149, CNRS EMR8252, Faculté de Médecine site Bichat, Université Paris Cité, Paris, France.

[5]Institut Cochin, INSERM U1016, CNRS UMR 8104, Université Paris Cité, Paris, France.

[6]Laboratory of Tumor Inflammation and Angiogenesis, Center for Cancer Biology, VIB, Leuven, Belgium.

[7]Laboratory of Tumor Inflammation and Angiogenesis, Center for Cancer Biology, Department of Oncology, KU Leuven, Leuven, Belgium.

[8] Roger Williams Institute of Liver Studies, School of Immunology & Microbial Sciences, Faculty of Life Sciences and Medicine, King's College London, Foundation for Liver Research and King's College Hospital, London SE5 9NU, UK.

[9]Dynamics of Immune Responses Unit, Institut Pasteur, Université Paris Cité, INSERM U1223, Paris 91401, France.

[10]INSERM U1015, Gustave Roussy Cancer Campus, Villejuif, 94800, France.

[11]Singapore Immunology Network (SIgN), Agency for Science, Technology and Research, Singapore, 138648, Singapore.

[12]Center for Immunity and Inflammation, Rutgers New Jersey Medical School, Newark, New Jersey, USA.

[13]Department of Pathology, Immunology and Laboratory Medicine, Rutgers New Jersey Medical School, Newark, New Jersey, USA.

[14]Immunology-Immunopathology-Immunotherapy (i3), UMRS 959, Sorbonne Université, INSERM, Paris, France.

[15]Université Paris Cité, Faculté de Médecine, Paris, France.

[16]Sorbonne Université, INSERM UMR-S 1166, 75013 Paris, France.

[17]Aix-Marseille University, CNRS, INSERM, CIML, Centre d'Immunologie de Marseille-Luminy, Turing Center for Living Systems, Marseille, France.

[18]Université de Paris Cité, PARCC, INSERM U970, 75006 Paris, France.

[19]Center for Immunity and Inflammation, Department of Pathology, Immunology, and Laboratory Medicine, New Jersey Medical School, Rutgers-he State University of New Jersey, Newark, NJ, USA.

[20]Champalimaud Research Program, Champalimaud Centre for the Unknown, Lisbon, Portugal.

[21]Barts Cancer Institute, Queen Mary University of London, London, UK.

[22]International Centre for Genome Engineering and Biotechnology, Trieste, Italy.

*These authors contributed equally to this work

§Corresponding author. pierre.guermonprez@pasteur.fr

ABSTRACT

The composition and diversity of tumor-infiltrating $CD8^+$ T cell populations have important consequences on the development of anti-tumor immunity. In a murine model of lung cancer, we have addressed the role of dendritic cell subsets on the generation of various types of tumor-infiltrating $CD8^+$ T cells. We show that $CD44^+PD1^-$ effector and $PD1^+TIM3^+$ exhausted, tumor-infiltrating $CD8^+$ T cells require $XCR1^+$ DC1s but not IRF4-dependent $CD11b^+$ DC2s. By contrast, immunotherapy responsive $CD103^+CXCR6^+$ T_{RM}-like, tumor-infiltrating $CD8^+$ T cells require both DC1s and DC2s. The same requirement is found in tumor-draining lymph nodes where we identify $CD103^+CXCR6^+$ T_{RM}-like precursors that are dependent on both $XCR1^+$ DC1s and $CD11b^+$, migratory DC2s. Mechanistically, we evidence that both types of migratory DCs cooperate. Mild TCR triggering by low MHCI-peptide density at the surface of cross-presenting migratory DC2s and low IL-12 support TGFb-dependent T_{RM} specification in lymph nodes. High TCR triggering and high MHCI-peptide density at the surface of cross-presenting migratory DC1s and high IL-12 support proliferative expansion and CXCR6 acquisition. Altogether, these findings highlight the induction of intratumoral T_{RM}-like cells under the collective aegis of multiple DCs subsets within tumor-draining lymph nodes reconciliating T_{RM} phenotype instruction with proliferative expansion.

MAIN

Tumor-infiltrating CD8$^+$ T cells (TILs) are critical mediators of anti-tumor immunity. CD8$^+$ TILs are characterized by the pervasive expression of exhaustion-associated features initially characterized in chronic infection models, including reduced proliferative response to TCR triggering and reduced polyfunctional cytokine responses. Multiple studies suggest that the qualitative composition of CD8$^+$ TILs in solid tumors predicts clinical outcome and response to immunotherapies[1,2]. In that line, a subset of CD8$^+$ TILs with a tissue-resident memory phenotype (T_{RM}) has been identified in solid tumors including lung and breast cancer and correlates with improved prognosis and better response to immunotherapies[1,3–9].

Bona fide T_{RM} have first been identified in peripheral tissues after clearance of viral infections[10]. Unlike other activated and memory CD8$^+$ T cells, T_{RM} do not recirculate but persist in tissues where they ensure immunosurveillance. T_{RM} are characterized by a specific transcriptional program including the expression of transcription factors Hobit (encoded by *Zfp683*), Runx3 and Blimp-1[4,11,12]. In some tissues, T_{RM} express αE integrin/CD103,which associates with integrin β7 to bind E-cadherin stabilizing contacts with epithelial cells, and low levels of S1P receptors ensuring tissue residency[13]. Also, T_{RM} stably express the CD69 lectin mediating S1P desensitization, further contributing to tissue residency[14].

Similar to *bona fide* anti-infectious T_{RM}, T_{RM}-like TILs harbor canonical features of residency including the concomitant expression of CD103, CD69, Hobit and reduced levels of S1PR1. A recent study in a murine model of E0771 murine breast tumors

suggests that CD69$^+$CD49a$^+$P2Rx7$^+$ T_{RM} phenotype within CD8$^+$ TILs may not indicate actual residency within tumors[15]. Still, several studies show that CD8$^+$ T_{RM}-like TILs cells can display potent anti-tumor function[16] as they secrete cytokines, exhibit cytotoxic activity[17] and can potentially generate a large repertoire of T cell subsets upon antigenic restimulation[18,19] or after immune checkpoint blockade[20]. T_{RM}-like TILs express some features of exhausted T cells but compared to T_{Exh}TILs, T_{RM}-like TILs display enhanced cytotoxicity and provide local protection in a murine model of breast cancer[20]. Consistently, numerous studies have identified a strong correlation between CD8$^+$ TILs with a T_{RM} phenotype and favorable outcomes and increased response rates to immune checkpoint inhibition in human lung cancer[1,3,5–7,9], triple-negative breast cancer and other solid tumors[16,21]. This calls for a better understanding of the mechanisms ensuring the acquisition of the T_{RM} program during T cell activation in solid tumors.

In cancer, CD8$^+$ T cells are initially activated in tumor-draining lymph nodes (tdLN) and terminally differentiate within the tumor[22,23]. However, the anatomical location where T_{RM}-like fate specification occurs in cancer is unclear (*i.e.*, during priming in tdLN or after infiltration in the TME). In a mouse model of skin vaccination, TGF-β activated by steady-state migratory DCs imprint an epigenetic state rendering naïve T cells poised to differentiate into T_{RM}[24]. Other studies identify T_{RM}-committed circulating progenitors during vaccination or viral infection, arguing in favor of early T_{RM} fate decision[25,26]. Anti-infectious T_{RM} can also be generated from circulating effector cells receiving T_{RM} instruction after tissue infiltration[4,27,28].

Dendritic cells (DCs) are the sentinel cells of the immune system ensuring T cell activation and differentiation. Classical DCs are diverse and composed of 2 main families expressing and relying on IRF8 or IRF4 transcription factors. There is wide evidence that IRF8$^+$, BATF3-dependent XCR1$^+$ DC1s control the activation of effector CD8$^+$ T cell responses in the context of immunogenic tumors[29–31] and maintain the fitness of CD8$^+$ T cell effector compartment by expanding TCF1$^+$ T cells in tdLN[32]. Efficient phagocytosis of tumor-derived cell debris and efficient cross presentation of cell-associated antigens by MHCI[33–35]and MHCII presentation to helper T cells[36] all support the paramount importance of XCR1$^+$ DC1s in shaping effector CD8$^+$ T cell responses. By contrast, the nature of antigen presenting DC subtypes controlling T_{RM} activation during T cell priming and infiltration is less clear and has mostly been investigated in the context of vaccination or infections. Skin XCR1$^+$ Batf3-dependent DC1s are essential for the efficient activation of skin T_{RM} after vaccination[37]. IRF4-dependent DC2s are essential for the priming of influenza-specific T_{RM} in lungs[38] and the maintenance of CXCR3$^+$ T_{RM} against HSV cervical infection[27]. Also, human IRF4$^+$CD163$^+$CD1c$^+$ DCs are the most potent antigen-presenting cells for T_{RM} specification *in vitro* or in humanized mice[39,40].

Despite numerous evidence of a role for CD8$^+$ T_{RM}-like TILs in non-small cell lung cancer (NSCLC) immunosurveillance[1,3,5–7,9,21], little is known on i) the anatomical location where the T_{RM}-like phenotype is specified and ii) if and how migratory DCs subsets participate to the induction of T_{RM}-like CD8$^+$ T cells within tumor-draining lymph nodes.

In this study, we delineate the activation of tumor-infiltrating T_{RM}-like cells in the KP (*Kras*^{G12D}, *p53*$^{-/-}$) model of lung adenocarcinoma. We identify an unexpected contribution

of IRF4-dependent migratory DCs in activating pre-T_{RM} precursors in tdLNs to give rise to tumor-infiltrating T_{RM}-like TILs. In addition, we show that the low density of MHCI-peptide complexes evoking a mild TCR triggering promote specification into T_{RM}-like phenotype.

RESULTS

CD8$^+$ T cells with a T_{RM}-like phenotype infiltrate lung tumors.

To determine the extent of T_{RM}-like cells infiltrating the lungs after engraftment of tumor cells, we employ a cell line derived from *Kras*^{G12D} *p53*$^{-/-}$ mice[32,41,42] (Fig.S1A). We found that a large proportion of CD8$^+$ TILs stained positive for both CD69 and CD103 expression (27.3%, Fig.1A) which is a classical gating for T_{RM} phenotype. CD8$^+$ TILs also stained positive for PD1 and TIM3 (21.7%, Fig.1B), a feature of exhausted T cells. In line with other studies highlighting the expression of exhaustion markers on T_{RM}-like TILs[3,20], we found that these two subsets were largely overlapping (Fig.1C and S1B). This led us to investigate the correspondence between cell surface phenotype and transcriptional profile in unbiased settings using a single-cell RNA-sequencing (scRNA-seq) combined with CITE-Seq approach (Fig. 1D and S1C). scRNA-seq identified 5 clusters of *Cd44*$^+$*Sell*$^-$ (coding respectively for CD44 and CD62L) cells (clusters 1, 4, 7, 8, 9) (Fig.1D-E and S1D). Clusters 4 expressed stemness genes, low level of *Pdcd1* (coding for PD1) and scored high for the Circulating signature, aligning it to recently extravasated from the blood, effector CD8$^+$T cells. Cluster 7 expressed stemness genes, intermediate levels of *Pdcd1* and intermediate score for Exhaustion module aligning it to a progenitor exhausted phenotype. Clusters 8 was the only cluster expressing high level of proliferation associated genes and scoring high for the Proliferation module, corresponding to a proliferative cluster. Clusters 1 and 9 expressed high levels of multiple exhaustion molecules (*Pdcd1, Havcr2/*Tim3, *Lag3, Tigit, Tox*) and scored high for an Exhaustion signature. Among these clusters, cluster 1 expressed core T_{RM}-associated genes (such

as *Itgae*/CD103, *Cd69*, *Itga1*/CD49a and *Cxcr6*) and scored high for Residency and T_{RM} signatures. Using CITE-Seq antibodies, we identified T_{RM}-like TILs ($CD44^+CD62L^-CD103^+CD69^+$) and found that they overlapped mostly with cluster 1 (Fig.1G and S1E). By contrast, cluster 9 was low for Residency and T_{RM} signatures. We, therefore, classified cluster 1 as T_{RM}-like and cluster 9 as terminally exhausted.

To further confirm these results, we designed a gating strategy enabling the prospective isolation of TILs populations identified above. As already shown previously, $CD69^+CD103^+$ T_{RM}-like TILs (cluster 1) were largely enriched in an exhausted phenotype $PD1^+TIM3^+$ (68.0%, termed here as $TIM3^+$ T_{RM}-like) but also contained a population of $PD1^+TIM3^-$ (29.2%, termed here as $TIM3^-$ T_{RM}-like) (Fig.1H-I). Conversely, we also identified $PD1^+TIM3^+$ (37.0%, termed here as $TIM3^+$ T_{Ex}, cluster 9) and $PD1^+TIM3^-$ (42.9%, termed here as $TIM3^-$ T_{Ex}, cluster 7) distinct from $CD69^+CD103^+$. PD1-negative $CD8^+$ T cells also comprised $CD62L^-CD44^+$ activated effector T cells (20.4%, termed here as $PD1^-$ T_{Eff}, cluster 4). Similar populations were found in the autochtonous KP cancer model which recapitulates the human physiopathology from hyperplasia to adenocarcinoma and the onset of T cell dysfunction[32,41–43] (Fig. S1F-I).

Bulk RNA-seq profiling further validated the correspondence between the T_{RM}-like gate and the enrichment in T_{RM}-associated genes and signatures (*Itgae*, *Itga1, Rgs1, Cxcr6 e.g.*) and gene ontology pathways “regulation of cell migration”, “TGF-β signalling pathway”, “R-SMAD binding” (Fig.1J-K and S1J-M). By contrast, T_{RM} expressed lower levels of effector-associated genes (*Eomes, Gzmk*, e.g.) and of genes ensuring recirculation (*Klf2* and *S1pr1, e.g.*)[4,11]. Finally, we confirmed by FACS that T_{RM}-associated

proteins (Hobit in Hobit reporter mice[18] and CD49a encoded by *Itga1*) were expressed at higher levels in TIM3$^+$ T_{RM} while they express low levels of EOMES and KLRG1 (Fig.1L-M). Also, we found that the human T_{RM} signature was enriched in TIM3$^+$ T_{RM}-like as compared to TIM3$^+$ T_{Ex} and in TIM3$^-$ T_{RM}-like as compared to TIM3$^-$ T_{Ex} (Fig.S1N), thereby showing the alignment of TILs in mouse lung KP tumors and human cancer. Unlike other T cell subsets, T_{RM}-like TILs (CD69$^+$CD103$^+$TIM3$^{+/-}$) were not stained after intravenous injection of anti-CD45.2-PE antibodies labelling the vascular compartment. This demonstrates their localization in the lung parenchyma (Fig.1N).

We next focused our analysis on tumor antigen-specific cells after engraftment of a KP cell line expressing the ovalbumin protein (KP-OVA, Fig.1O-P). Tumor-antigen specific tetramer-OVA$^+$ cells (Tet-OVA$^+$) encompassed similar subsets but displayed a significant enrichment in TIM3-expressing cells including both TIM3$^+$ T_{Ex} and TIM3$^+$ T_{RM}-like, unlike PD1$^-$ T_{Eff} that were mostly found in the Tet-OVA$^-$ fraction (Fig.1P-R and Fig.S2D-E). Similar results were found in the AT3-OVA orthotopic model of breast cancer (Fig.S2A-C). Functionally, we found that both TIM3$^+$ T_{RM}-like (15.5%) and TIM3$^+$ T_{Ex} (11.9%) were able to produce pro-inflammatory cytokines IFNγ and TNFα after *ex vivo* antigen-specific restimulation with the $OVA_{257-264}$ peptide (Fig.S2F). Moreover, both T_{Ex} and T_{RM}-like exert cytotoxicity and release granzyme B during *ex vivo* co-culture assays with KP-OVA tumors (Fig.S2G). However, T_{RM}-like containing cultures demonstrate higher IFNγ release as compared to T_{Ex}. We next sought to determine if T_{RM}-like would respond to immune checkpoint blockade (ICB). To this end, we analyzed KP TILs in mice treated with anti-PD-1 and anti-CTLA-4 antibodies alone or in combination (Fig.S2H-J). We found

206 that combination treatment induced a relative expansion of TIM3$^-$ T_{RM}-like as compared
207 to other CD8$^+$ TILs. Acute exposure to anti-PD-1 was sufficient to increase the percentage
208 of polyfunctional IFNγ$^+$TNFα$^+$ cells in all TIM3$^+$ TILs, resulting in the most efficient cytokine
209 production in TIM3$^+$ T_{RM}-like as compared to TIM3$^+$ T_{Ex}. (Fig. S2K-M).

210 Altogether, we conclude that the transplanted KP model recapitulates some features of
211 human NSCLC in terms of partial dysfunctionality and T_{RM}-like phenotype[1,3,7,9,44]. Our
212 results define T_{RM}-like TILs as a specific, separable subset within a larger population of
213 CD8$^+$ TILs expressing co-inhibitory receptors. Therefore, this model is suitable to
214 investigate how the T_{RM}-like phenotype is instructed in comparison to other TILs.

Figure 1 - T_{RM}-like CD8$^+$ T cells infiltrate lung tumors

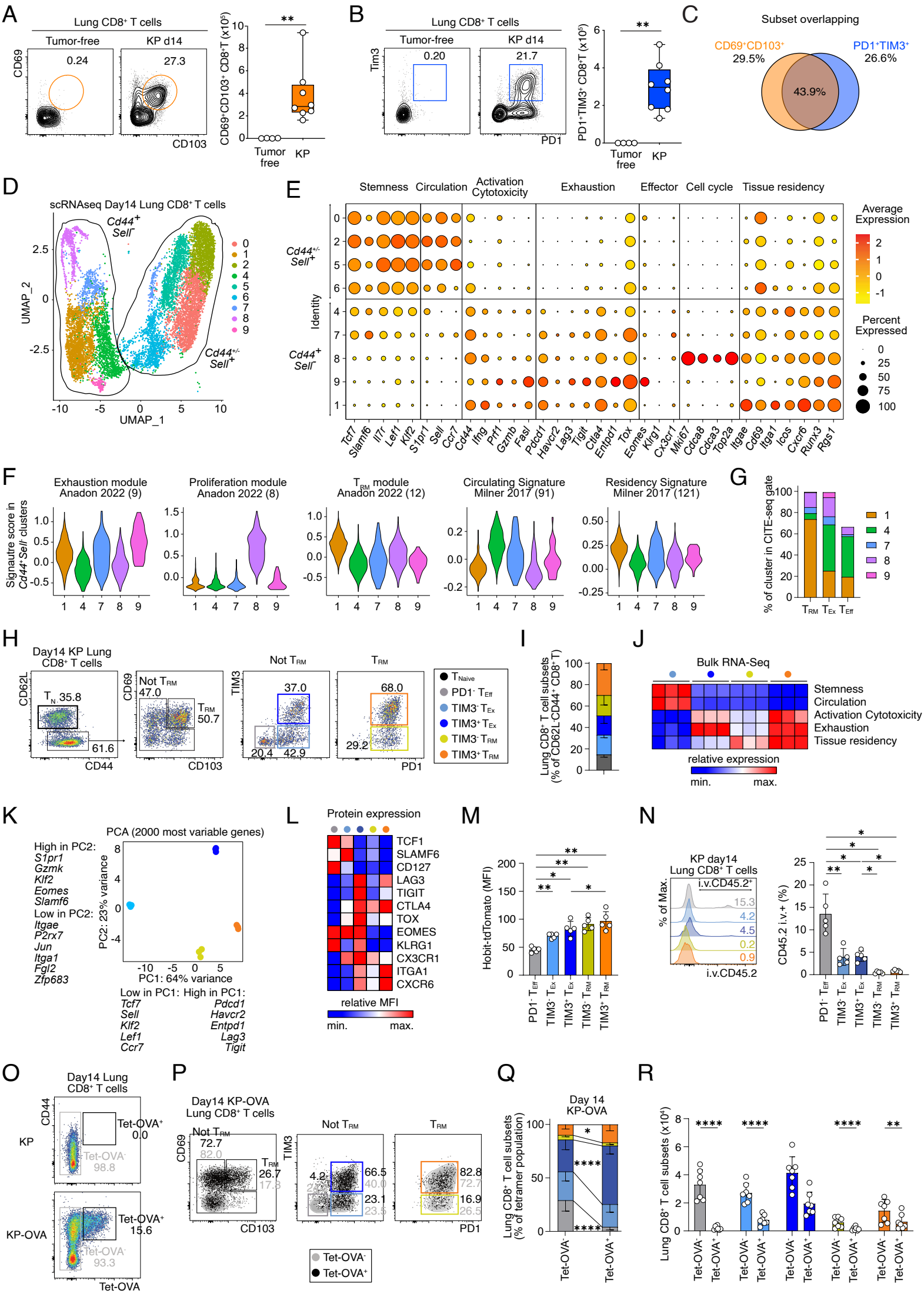

Fig. 1. T_{RM}-like $CD8^+$ T cells infiltrate lung tumors.

(**A-B**) Representative flow cytometry plots and quantifications of $CD69^+CD103^+$ $CD8^+$ T_{RM} (A) and exhausted $PD1^+TIM3^+$ $CD8^+$ T cells (B) in the lungs of tumor-free and KP tumor-bearing mice 14 days post-tumor cells injection (n = 4 tumor-free and n = 8 KP mice, unpaired t-tests).

(**C**) Venn diagram showing the overlap between $CD69^+CD103^+$ and $PD1^+TIM3^+$ $CD8^+$ T cells in the lungs of KP-tumor bearing mice 14 days post-tumor cells injection (n = 8 mice).

(**D-G**) scRNAseq analysis of sorted total lung $CD8^+$ T cells from KP-bearing mice 14 days post-tumor cells injection (see also Fig.S1C).

(**D**) UMAP dimensionality reduction embedding the different clusters.

(**E**) DotPlot showing the RNA expression of core marker genes across clusters.

(**F**) Violin Plots showing the scoring of indicated gene signatures across *Cd44*$^+$*Sell*$^-$ clusters[4,11,16].

(**G**) Distribution of *Cd44*$^+$*Sell*$^-$ clusters across CITE-Seq gated $CD44^+CD62L^-$ $PD1^+CD69^+CD103^+$ T_{RM}, $CD44^+CD62L^-PD1^+$Not($CD69^+CD103^+$) T_{Exh} and $CD44^+CD62L^-$ $PD1^-$ T_{Eff}.

(**H**) Representative flow cytometry gating strategy used to identify $CD8^+$ T cell populations infiltrating lung KP tumors.

(**I**) Quantification of the proportions of $CD62L^-CD44^+$ $CD8^+$ T cell populations infiltrating lung KP tumors (n = 10 mice).

(**J-K**) Bulk RNA-sequencing analysis of sorted $CD8^+$T cell populations as defined in Figure 1H.

(**J**) Signature scoring of gene modules related to stemness, circulation, activation-cytotoxicity, exhaustion and tissue-residency as shown in Figure S1L.

(**K**) Principal-component analysis (PCA). Top high and low loading genes are indicated for PC1 and PC2.

(**L**) Relative MFI protein expression of indicated marker genes across $CD8^+$ T cell populations as determined by flow cytometry in Figure 1H.

(**M**) Hobit-tdTomato MFI expression across lung $CD8^+$ T cell populations quantified in Hobit-tdTomato reporter mice[18] bearing KP tumors (n = 5 mice, paired one-way anova).

(**N**) Representative histogram and quantifications of CD45.2-labelled cells following intravenous injection of a CD45.2-fluorescent antibody 5min before sacrifice (n = 5 mice, paired one-way anova).

(**O**) Representative flow cytometry plots showing the gating of tetramer-OVA^+ $CD8^+$ T cells infiltrating KP-OVA but not KP lung tumors.

(**P**) Representative flow cytometry gating strategy showing the phenotype of tetramer-OVA^+ (dark) or tetramer-OVA^- cells (grey) infiltrating KP-OVA lung tumors.

(**Q-R**) Quantification of the proportions (Q) or absolute numbers (R) of Tet-OVA^+ or Tet-OVA^- $CD8^+$ T cell populations infiltrating lung KP-OVA tumors (n = 6 mice, paired two-way anova).

Tumor-draining lymph nodes contain a fraction of CD103$^+$ activated CD8$^+$ T cells poised to generate T_{RM}-like TILs.

The anatomical localization where T_{RM} specification occurs is still a matter of debate. Therefore, we wondered whether CD8$^+$ T_{RM}-like TILs require egress from tumor-draining mediastinal lymph nodes (tdLN) or differentiate *in situ* from a T cell pool pre-existing tumor development. To address this, we inhibited lymph node egress using S1PR1 blockade with fingolimod (FTY720) and analysed T_{RM}-like TILs at day 14 post-tumor engraftment (Fig.2A). We found that FTY720 administration from day 1 to 14 or from day 7 to 14 blocked T_{RM} infiltration in the lungs (Fig.2B). We conclude that tdLNs represent an obligate site during the development of CD8$^+$ T_{RM}-like TILs.

Having established a role for tdLN in T_{RM} infiltration, we next sought to characterize tdLN CD8$^+$ T cells after KP tumor engraftment. We found that KP tumor development induced the expansion of CD62L$^-$CD44$^+$ activated CD8$^+$ T cells (T_{Act}) (Fig.2C and S3A-D). Because CD103 expression has been widely used as a marker of T_{RM} biased T cells in other settings[24], we analysed CD103 expression and found that 41.3% of T_{Act} expressed CD103 (Fig.2C and S3A-B). KP tumors induced a large expansion of CD103$^+$ and CD103$^-$ T_{Act} (Fig.2D). CD103$^+$ T_{Act} population was similarly observed in OVA-specific T_{Act} after KP-OVA engraftment (15.0%) (Fig.2E-F and S3E). Bulk RNA-sequencing analysis showed that CD103$^+$ T_{Act} were enriched in T_{RM} core genes such as *Cxcr6, Fgl2, Itga1* and *Innp4b* (Fig.2G and S3F-H). On the contrary, CD103$^-$ T_{act} expressed more effector genes (*Eomes*, *Gzmk*) and proliferation-associated genes (*Mki67*). Consistently, GSEA analysis revealed that lymphocyte residency signatures were enriched in CD103$^+$ T_{Act} while

signature of genes associated to circulating lymphocytes were enriched in CD103$^-$ T_{Act}[4,11] (Fig.S3I-J). CD103$^+$ T_{Act} were also enriched for genes associated to KP-bearing lung TIM3$^+$ T_{RM}-like while CD103$^-$ T_{Act} were enriched for genes associated to KP bearing-lung TIM3$^+$ T_{Ex} (Fig.2H). At the protein level, CD103$^+$ T_{Act} expressed lower levels of effector-associated markers (T-BET, EOMES, KLRG1 and CX3CR1) (Fig.2I) but higher T_{RM}-enriched markers such as CD49a, Hobit, CTLA4 and CXCR6 (Fig.2J and S3L). We therefore hypothesized that CD103$^+$ T_{Act} are biased to give rise to lung T_{RM}-like TILs. To assess the relationship between CD103$^+$ T cells in tdLN and lung T_{RM}-like TILs, we took advantage of the *CD103-cre^{ERT2}-ROSA$^{LSL\text{-}tdTomato}$* reporter mouse[45] (hereafter referred as CD103-tdTomato). Tamoxifen induction efficiently labelled CD103$^+$ T_{Act} (45.6%) but not CD103$^-$ T_{Act} (1.5%) in tdLNs from CD103-tdTomato donor mice (Fig.2M). As a result, 84.7% of tdTomato$^+$ cells stained positive for CD103, validating labelling specificity (Fig.2L). We thus transferred whole CD45.2$^+$ tdLN containing genetically labelled CD103$^+$ T cells in KP tumor-bearing CD45.1$^+$ WT recipient mice and assessed T_{RM} phenotype in the progeny of tdTomato$^-$ or tdTomato$^+$ transferred tdLN CD8$^+$ T cells in the lungs (Fig.2K-P and S3M-O). We found that CD45.2$^+$ tdTomato$^+$ transferred T cells predominantly gave rise to T_{RM}-like but barely no other CD44$^+$CD62L$^-$ CD8$^+$ TILs (67.0%, Fig.2N-P and S3N-O). By contrast, only a minor fraction of tdTomato$^-$ transferred CD8$^+$ T cells differentiated into T_{RM}-like TILs (7.0% of CD44$^+$CD62L$^-$ CD8$^+$ TILs).

These results demonstrate that T_{RM} specification is initiated in tdLNs where CD103$^+$ T_{Act} cells are pre-committed to differentiate into T_{RM}-like TILs after seeding tumor-bearing lungs.

Figure 2 - Tumor-draining lymph nodes contain a fraction of CD103⁺ activated CD8⁺ T cells poised to generate T_{RM}-like TILs

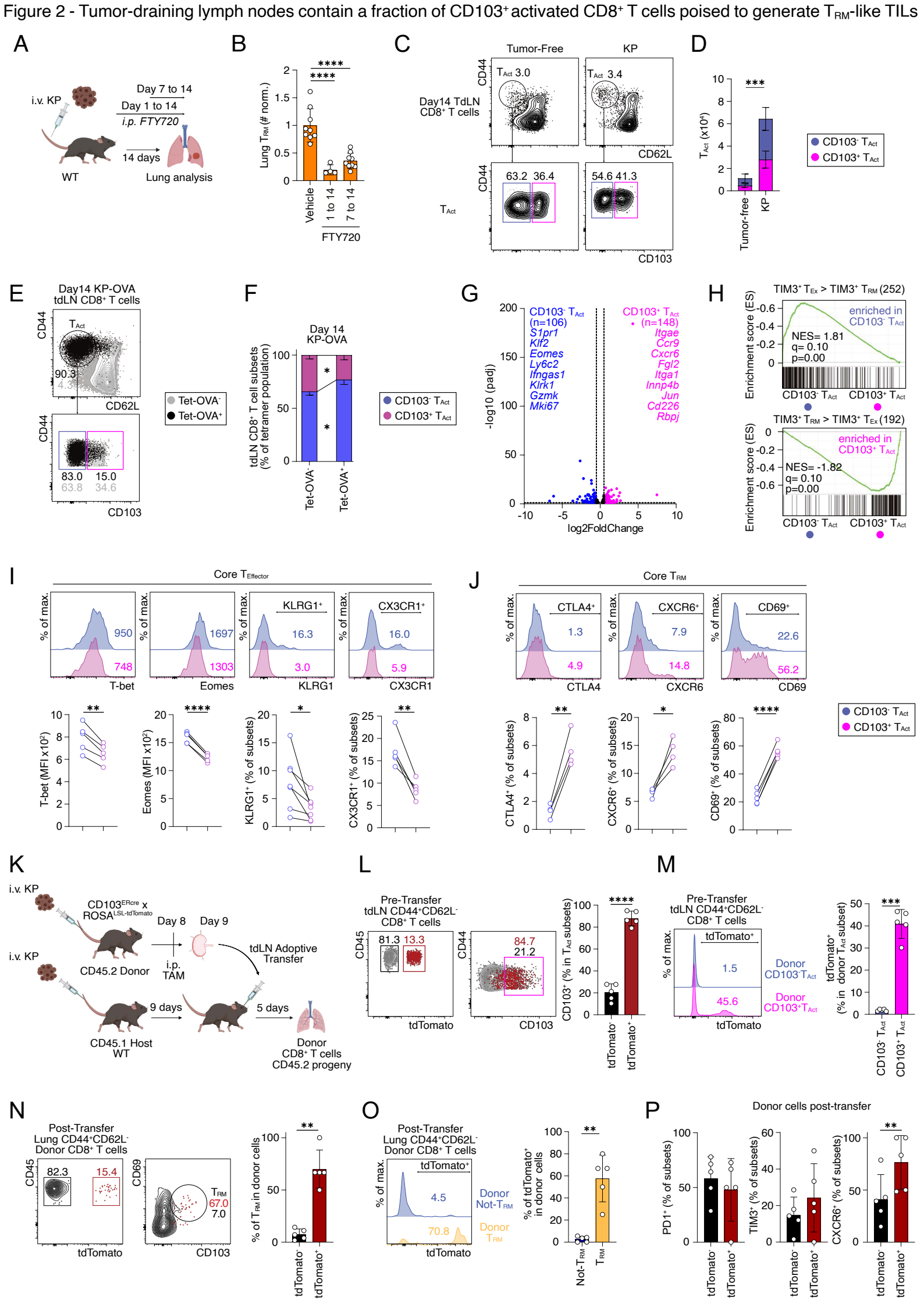

Fig. 2. Tumor-draining lymph nodes contain a fraction of CD103$^+$ activated CD8$^+$ T cells poised to generate T_{RM}-like TILs.

(**A**) Experimental design for T cell trapping in the LN. Mice were injected i.v. with KP tumors. Mice were treated with vehicle or FTY720 to block lymphocyte egress from all lymphoid tissues every 2-3 days from day 1 or from day 7 post-KP-injection.

(**B**) Quantification of T_{RM} after FTY720 treatment at day 14 post-KP-injection (n = 9 vehicle, n = 4 FTY720 mice day 1 to 14 and n = 9 FTY720 day 7 to 14 mice, unpaired one-way anova).

(**C-D**) Representative flow cytometry plots (C) and quantification (D) of CD103$^+$ and CD103$^-$ T_{Act} in the mediastinal LN of tumor-free and KP-tumor bearing mice (n = 3 naïve and n = 8 KP mice, unpaired t-test).

(**E-F**) Representative flow cytometry plots (E) and quantification (F) showing the phenotype of tetramer-OVA$^+$ (dark) or tetramer-OVA$^-$ cells (grey) in the tdLN of KP-OVA tumor bearing mice (n = 5 KP mice, paired two-way anova).

(**G**) Volcano plot representing differentially expressed genes between CD103$^+$ T_{Act} and CD103$^-$ T_{Act}. Genes with Log2(fold change, FC) > ±2 and a false discovery rate (FDR)-adjusted p value of less than 0.05 were considered significant.

(**H**) GSEA of pairwise comparisons of CD103$^+$ T_{Act} vs CD103$^-$ T_{Act} using differentially expressed genes between lung TIM3$^+$ T_{RM} and TIM3$^+$ T_{Ex}.

(**I-J**) Flow cytometry quantifications of $T_{effector}$ (I) and T_{RM} (J) core markers in CD103$^-$ T_{Act} and CD103$^+$ T_{Act} (n = 4-7 mice, paired t-tests). Median fluorescent intensity was calculated for transcription factors and percentage of positivity for membrane proteins.

(**K-P**) Adoptive transfer of total tdLN from CD103^{ERcre} x ROSA$^{LSL\text{-}tdTomato}$ mice.

(**K**) Experimental design. Donor CD45.2^{+} CD103^{ERcre} x ROSA$^{LSL\text{-}tdTomato}$ and host WT CD45.1^{+} mice were injected with KP cells. 8 days later, tomato labelling was induced in donor mice by intraperitoneal injection of tamoxifen. At day 9, donor tdLNs were transferred intravenously in host mice (i.e., each total donor tdLN was transferred into one recipient mice). Lungs from host mice were analyzed 5 days post-transfer to assess the progeny of tdTomato-labelled transferred cells.

(**L-M**) Representative flow cytometry plots and quantification of the percentage of CD103^{+} within donor tdTomato^{-} or tdTomato^{+} T_{Act} (L) or, conversely, the percentage of tdTomato^{+} within CD103^{-} or CD103^{+} T_{Act} (M) in tdLN pre-transfer (n = 5 mice, paired t-tests).

(**N-O**) Representative flow cytometry plots and quantification of the percentage of T_{RM}-like within donor tdTomato^{-} or tdTomato^{+} CD44^{+}CD62L^{-}CD8^{+}T (N) or, conversely, the percentage of tdTomato^{+} within donor T_{RM}-like or not-T_{RM} (M) in recipient lungs post-transfer (n = 5 mice, paired t-tests).

(**P**) Quantifications of the expression of PD1, TIM3 and CXCR6 within donor tdTomato^{-} or tdTomato^{+} in recipient lungs post-transfer (n = 5 mice, paired t-tests).

CD103$^+$ activated T cells in tdLN contain a tumor antigen-specific population of CXCR6$^+$ T_{RM} precursors.

To better characterize the heterogeneity of tdLN activated CD103$^+$CD8$^+$T cells giving rise to lung T_{RM}-like TILs in unbiased settings, we performed single-cell RNA-sequencing of a mixture of 80% of T_{Act} and 20% of T_{Naive} and T_{CM} (Fig.3A and S4A). We identified 4 clusters of activated *Cd44*$^+$*Sell*$^-$ CD8$^+$ T cells (clusters 0, 3, 5 and 8)(Fig. 3B-C and S4B). Cluster 5 was highly proliferating (*Mki67*^{high}). Among the remaining activated clusters, *Itgae* expression was restricted to clusters 0 and 8. Strikingly, cluster 8 expressed high levels of *Cxcr6* and scored high for residency but low for circulating signatures or stemness-associated genes (*Slamf6, Tcf7*)(Fig.3B-C). Consistently, this cluster scored the highest for genes associated to KP-bearing lung TIM3$^+$ T_{RM} (Fig.S4B). CITE-Seq gating also showed that CD103 was most highly expressed by cluster 8 (Fig.S4C). However, the majority of CD103$^+$ T_{Act} cells were found in cluster 0 since cluster 8 contains very few cells (Fig.3D). Of note, *Sell*$^+$ cells contained a cluster of CD103$^+$ T cells (cluster 4) which might represent preconditioned naïve progenitors as described in other studies[24,46]. To further compare single-cell RNA-seq clusters obtained in both lung and tdLN locations, we projected lung clusters on the tdLN dataset. We found that T_{RM} cluster 1 from the lung was almost exclusively projected on *Cxcr6*$^+$ cluster 8 from the tdLN (84.25%, Fig.3E), thereby validating their transcriptional alignment. Taking advantage of this information, we refined our FACS gating strategy to separate previously gated CD103$^+$ T_{Act} into CD103$^+$CXCR6$^-$ and CD103$^+$CXCR6$^+$ T_{Act} (Fig.3F). We found that CD103$^+$CXCR6$^+$ T_{Act} expressed low levels of SLAMF6 but higher levels of PD1, CD49a

and Hobit than CD103$^-$ or CD103$^+$CXCR6$^-$ T_{Act} (Fig.3G and S4D). CD103$^+$CXCR6$^+$ T_{Act} were found highly enriched within tumor antigen-specific Tet-OVA$^+$ T_{Act} from KP-OVA bearing mice (4.2% of Tet-OVA$^-$ T_{Act} vs 16.9% of Tet-OVA$^+$ T_{Act}) (Fig.3H-J and S4E). Phenotyping Tet-OVA$^+$ T_{Act} led to similar results compared to polyclonal T_{Act} as CD103$^+$CXCR6$^+$ T_{Act}expressed high levels of T_{RM} marker CD49a but low levels of SLAMF6 (Fig.S4F-G). Similar results were obtained in the AT3-OVA orthotopic breast tumor model in which tumor-specific CD8$^+$ T cells contained a large CD103$^+$CXCR6$^+$ fraction (39.4% of Tet-OVA$^+$ T_{Act}) (Fig.S4I-K).

In order to identify conserved T_{RM} markers across anatomical locations in the KP model, we combined our different datasets and found that 38 genes overlapped between lung T_{RM}-like cluster 1, tdLN *Cxcr6*$^+$ cluster 8 and genes associated to lung TIM3$^+$ T_{RM}-like as compared to TIM3$^+$ T_{Ex} (Fig.S4L). We validated at the level of protein expression that JAML, DNAM (encoded by *Cd226*) and CD49a were indeed expressed at higher levels by lung T_{RM} and tdLN CD103$^+$CXCR6$^+$ T_{Act} as compared to other CD8$^+$T cell subsets (Fig.S4M).

We next assessed if ICB immunotherapy would impact on the CD103$^+$CXCR6$^+$ T_{Act} compartment. We found that chronic anti-PD-1 and anti-CTLA-4 synergized to increase the frequency of CD103$^+$CXCR6$^+$ within tdLN Tet-OVA$^+$ T_{Act} (Fig.3K-L). Together, these results demonstrate the existence of a tumor antigen-specific population of CD103$^+$CXCR6$^+$ T_{RM}-like precursors in tdLN.

Figure 3 - CD103⁺ activated T cells in tdLN contain a tumor antigen-specific population of CXCR6⁺ T_{RM} precursors

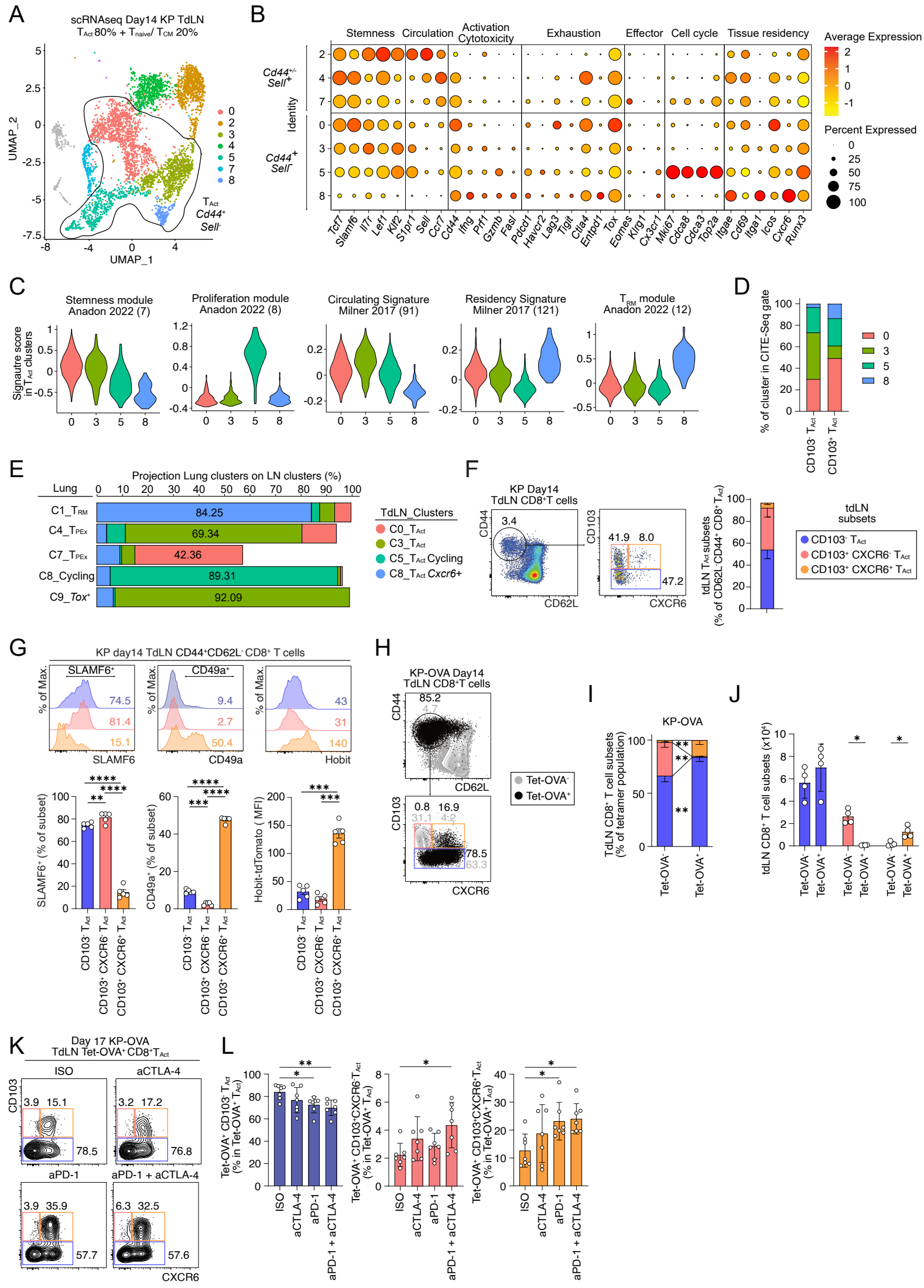

Fig. 3. CD103$^+$ activated T cells in tdLN contain a tumor antigen-specific population of CXCR6$^+$ T_{RM} precursors.

(**A-E**) scRNAseq of 80%T_{Act} and 20% T_{CM}/T_{Naive} sorted from the tdLN of 14 days KP-bearing mice (gating strategy in Figure S4A).

(**A**) UMAP dimensionality reduction embedding the different clusters.

(**B**) Dot Plot showing the expression of core marker genes across clusters.

(**C**) Violin Plots showing the scoring of indicated gene signatures across activated clusters[4,11,16].

(**D**) Distribution of T_{Act} clusters across CITE-Seq gated CD103$^-$ T_{Act} and CD103$^+$ T_{Act}.

(**E**) Projection of lung *Cd44$^+$Sell$^-$* scRNA-seq clusters 1, 4, 7, 8 and 9 on tdLN T_{Act} clusters 0,3,5 and 8.

(**F**) Representative flow cytometry gating strategy to identify T_{Act} populations and associated quantification (n = 12 mice).

(**G**) Representative flow cytometry histograms and quantifications of SLAMF6 and Hobit-tdTomato expression across tdLN T_{Act} subsets (n = 5 Hobit-tdTomato mice, paired one-way ANOVA test).

(**H**) Representative flow cytometry gating strategy showing the phenotype of tetramer-OVA$^+$ (dark) or tetramer-OVA$^-$ cells (grey) in the tdLN of KP-OVA tumor bearing mice.

(**I-J**) Quantification of the proportions (I) and absolute numbers (J) of Tet-OVA$^+$ or Tet-OVA$^-$ CD8$^+$ T cell populations in the tdLN of KP-OVA tumor bearing mice (n = 4 mice, paired two-way anova).

(**K-L**) Representative flow cytometry plots (**K**) and quantifications (**L**) of the proportions of each T_{Act} subset within tdLN Tet-OVA^{+} CD8^{+} T cells at day 17 post KP-OVA tumor injection and chronic isotype, anti-PD-1, anti-CTLA-4 or combined treatment as depicted in Figure S2K.

Both XCR1$^+$ and CD11b$^+$ DCs contribute to the differentiation of T_{RM} precursors in tdLN

Because DCs are the main tumor antigen-presenting cells in the LN, we assessed their requirements for the generation of T_{RM}-like precursors in tdLN. We found that KP tumor development triggered a massive increase of both resident and migratory XCR1$^+$ DC1s and CD11b$^+$ DC2/3s compared to mediastinal LN from naïve mouse (Fig.4A-C and S5A). To better characterise DC populations in tdLN, we performed scRNA-Seq of CD11c$^+$MHCII$^+$ cells 14 days after KP tumor engraftment (Fig.S5B-D). We identified 2 clusters of resident DC1 (clusters 7, 14) and 3 clusters of resident DC2 (clusters 3, 9 ,17). Within the clusters expressing high levels of maturation markers (*Ccr7*, *Cd80, Cd86, Cd200, Cd274, Pdcd1lg2 e.g.*) (clusters 2, 5, 8), CITE-Seq protein expression of XCR1 and SIRPα, respectively expressed in DC1 and DC2, enabled to discriminate migratory DC1 (cluster 8) from migratory DC2 (cluster 2), although cluster 5 was composed of a mix of migratory DC1 and DC2 as reported earlier[47] (Fig.S5F). Migratory DC2s (cluster 2) expressed *Irf4* (Fig.S5E). Fate mapping experiments using *Zbtb46^{cre}xRosa$^{LsL\text{-}tdTomato}$* mice demonstrated that most migratory DC2/3s belong to the classical DC lineage[48] (73.2%) (Fig.S5G). By contrast, only a minor fraction of migratory DC2/3s stained positive in GMP/DC3s labelling *Ms4a3^{cre}xRosa$^{LsL\text{-}dTomato}$*,[49] (11.4%) (Fig.S5H) or *LyzM^{cre}xRosa$^{LsL\text{-}dTomato}$*,[50] (33.0%) (Fig.S5I). These results identified migratory CD11b$^+$ DCs as a mixture of *bona fide* DC2s and DC3-related phenotypes. For convenience, DC2/3 will be termed as DC2s hereafter. To assess the contribution of DC subsets in T_{RM} differentiation, we engrafted KP-OVA tumors in *Xcr1^{cre}xRosa$^{LsL\text{-}DTA}$* (*XCR1*^{DTA};[51]) or *Itgax*^{cre}x*Irf4*$^{fl/fl}$

(*CD11c*^{IRF4};[52]) mice. *XCR1*^{DTA} mice were deficient in DC1s while *CD11c*^{IRF4} mice had reduced numbers of migratory but not resident DC2s (Fig.4D and S5J-K). By performing scRNA-seq in *CD11c*^{IRF4}mice, we confirmed that migratory DC2 cluster 2 was reduced as compared to WT mice, while most clusters including resident DC2 clusters 3, 9 and 17 were left unaffected (Fig.S5L-M). Consistent with a well-established role of DC1s in activating CD8$^+$ T cell responses[29,30,53,54], we found that Tet-OVA$^+$ T_{Act} were severely reduced in *XCR1*^{DTA} mice bearing KP-OVA tumors, including CD103$^+$ T_{Act} (Fig.4E-F and S5N). Conversely, depletion of IRF4-dependent DCs in *CD11c*^{IRF4} mice did not impact Tet-OVA$^+$ CD8$^+$ T cell activation but led to a selective decrease in Tet-OVA$^+$CD103$^+$ T_{Act} numbers. Similar results were found after adoptive transfer of OT-1, OVA-specific transgenic CD8$^+$T cells, prior to tumor engraftment (Fig.S5O). Analysis of OT-1 in tdLN at day 9 revealed impaired CD103 expression in both *XCR1*^{DTA}and *CD11c*^{IRF4}mice (Fig.4G-H). We thus wondered whether CD103$^+$CXCR6$^+$ T_{Act} would be selectively affected by lack of DC populations in *XCR1*^{DTA} and *CD11c*^{IRF4} mice bearing KP tumors. We found that all T_{Act} populations including CD103$^+$CXCR6$^+$ T_{Act} were severely reduced in *XCR1*^{DTA} mice (Fig.4I-K). By contrast, total T_{Act} numbers were similar in *CD11c*^{IRF4} mice, but both CD103$^+$CXCR6$^-$ and CD103$^+$CXCR6$^+$ T_{Act} were reduced. Similar results were obtained in AT3-OVA breast tumors in which the absence of DC1 in *XCR1*^{DTA} mice broadly impact the activation of all CD8$^+$ T cells in tdLNs (Fig.S6A-B and S6E-G). Impairment of migratory DC2s in *CD11c*^{IRF4} mice resulted in a decrease in CD103$^+$CXCR6$^+$ T_{Act}, although total Tet-OVA$^+$ T_{Act} were also impacted (Fig.S6C-D and S6H-J).

We next sought to validate these findings using an alternative method to deplete migratory DC2s. Because migratory DC2s specifically expressed the MGL2 lectin (Fig.S5P), we used *Mgl2*^{DTR} mice[55] to deplete them. Upon DT administration, a wide proportion of migratory DC2s were depleted (Fig.4L). As a consequence, only tumor-specific Tet-OVA$^+$ CD103$^+$CXCR6$^-$ and CD103$^+$CXCR6$^+$ T_{Act} subsets were reduced in KP-OVA tdLNs, while CD103$^-$ Tet-OVA$^+$ T_{Act} were left unchanged (Fig.4M-O). Of note, *XCR1*^{DTA} but not *CD11c*^{IRF4} mice displayed increased tumor growth in the KP-OVA and AT3-OVA models (Fig.S5Q and S6A-D).

Altogether, these results demonstrate that:

- DC1s have a non-redundant function in the activation of all tumor-specific CD8$^+$ T cell populations.
- Both DC1s and migratory DC2s are required for the differentiation of CD103$^+$CXCR6$^+$ T_{RM}-like precursors in tdLN.

Figure 4 - Both XCR1⁺ and CD11b⁺ DCs contribute to the differentiation of T_{RM} precursors in tdLN

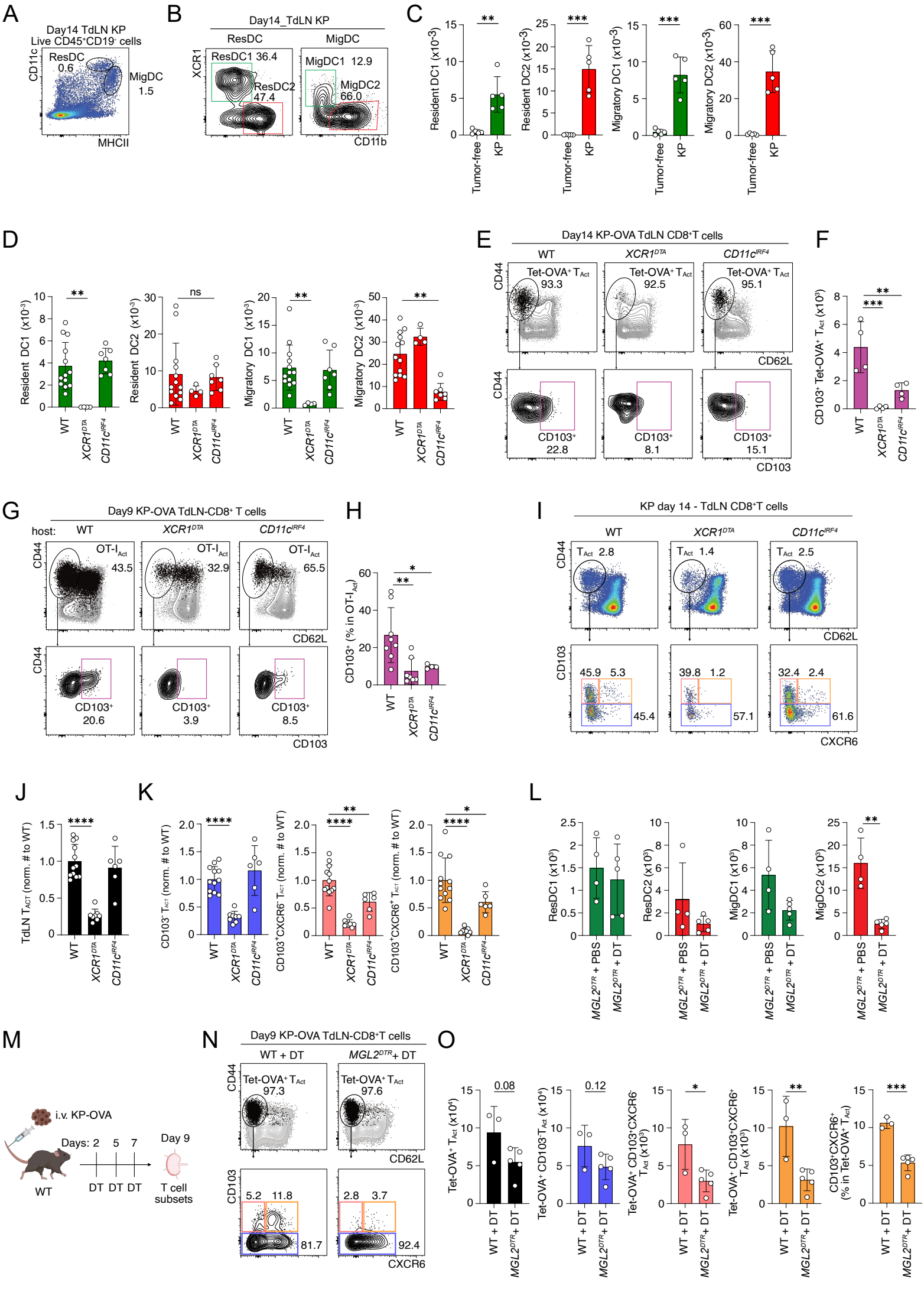

Fig. 4. Both XCR1^{+} and CD11b^{+} DCs contribute to the differentiation of T_{RM} precursors in tdLN.

(**A**) Representative flow cytometry plot for the gating of CD11c^{high}MHCII^{int} resident vs CD11c^{int}MHCII^{high} migratory dendritic cells in tdLNs of KP tumor-bearing mice.

(**B-C**) Representative flow cytometry plots for the gating of migratory and resident DC1 and DC2 (B) and quantification (C) in tumor-free or KP tumor-bearing mice (n = 5 tumor-free and n = 5 KP mice, unpaired t-tests)

(**D**) Quantification of resident DC1, resident DC2, migratory DC1 and migratory DC2s in WT, *XCR1*^{DTA} and *CD11c*^{IRF4} mice bearing KP tumors (n = 13 WT, n = 4 *XCR1*^{DTA} and n = 7 *CD11c*^{IRF4} mice, one-way anova).

(**E-F**) Representative flow cytometry plots (E) and quantification (F) of CD103^{+} and CD103^{-} tetramer-OVA^{+} T_{Act} in the tdLN of WT, *XCR1*^{DTA} and *CD11c*^{IRF4} mice bearing KP-OVA tumors (n = 4 WT, n = 4 *XCR1*^{DTA} and n = 4 *CD11c*^{IRF4} mice, one-way anova). Black tetramer-OVA^{+} cells overlay grey tetramer-OVA^{-} cells.

(**G-H**) Representative flow cytometry plots and quantifications of transferred tdLN CD103^{+} OT1 as described in Figure S5O. Black CD45.1^{+} OT1 overlay grey endogenous CD45.2^{+} CD8^{+} T cells.

(**I-K**) Representative flow cytometry plots (**I**) and quantifications of total T_{Act} (**J**) or T_{Act} subsets (**K**) in WT, *XCR1*^{DTA} or *CD11c*^{IRF4} mice bearing KP-tumors (n = 12 WT, n = 8 *XCR1*^{DTA} and n = 6 *CD11c*^{IRF4} mice, one-way ANOVA tests).

(**L**) Quantification of resident DC1, resident DC2, migratory DC1 and migratory DC2s in KP-bearing *Mgl2*^{DTR} mice treated with PBS or diphteria toxin at day 8 and analyzed at

day 9 post-KP tumor injections (n = 4 *Mgl2*^{DTR} + PBS and n = 4 *Mgl2*^{DTR} + DT mice, unpaired t-test).

(**M-O**) WT or *Mgl2*^{DTR} mice bearing KP-OVA tumors were treated with diphteria toxin at days 2, 5 and 7 and analyzed at day 9.

(**M**) Schematic of the experiment

(**N-O**) Representative flow cytometry plots (N) and quantifications (O) of tdLN tetramer-OVA^{+} T_{Act} subsets (n = 3 WT + DT and n = 5 *Mgl2*^{DTR} + DT mice, unpaired t-test). Black tetramer-OVA^{+} cells overlay grey tetramer-OVA^{-} cells.

Efficient generation of T_{RM}-like TILs requires both DC1s and DC2s at the level of tdLN.

We next sought to address the consequences of impaired T_{RM} specification at the level of tdLN on the generation of lung T_{RM}-like TILs.

In a first approach, we engrafted KP tumors in WT, *Flt3L*$^{-/-}$ deficient in all classical DC subsets, and *Ccr2*$^{-/-}$ mice deficient in inflammatory monocytes and assessed CD8$^+$ T_{RM}-like content. In accordance with a non-redundant role of classical DCs in CD8$^+$ T cell immunity[29,48], we found that infiltration of all PD1$^+$ activated CD8$^+$ T cell subsets including T_{RM}-like was deeply inhibited in DC-deficient *Flt3L*$^{-/-}$ mice (Fig.S7A-B). However, T_{RM}-like TILs accrual was not modified in *Ccr2*$^{-/-}$ mice, excluding a role for monocyte-derived/inflammatory phagocytes in T_{RM}-like generation. To further define the role of DC1 and DC2, we analysed the differentiation of polyclonal CD8$^+$T cells in *XCR1*^{DTA} and *CD11c*^{IRF4} mice engrafted with KP tumors. In *XCR1*^{DTA} mice, a major defect in the infiltration of all CD8$^+$ T cells subsets was observed (Fig.5A-B). These results highlight general defects in CD8$^+$ T cell activation in DC1-lacking mice[29,32,54] and correlate with the deep impairment in T cell activation observed in tdLN (Fig.4E-K). By contrast, *CD11c*^{IRF4} mice only had a partial and selective defect in both TIM3$^-$ and TIM3$^+$ T_{RM}-like populations while other populations of CD8$^+$ TILs were left unaffected.

Next, we intended to address the role of DC subsets on CD8$^+$ T cell populations in tumor antigen-specific settings using KP-OVA tumors engrafted in WT, *XCR1*^{DTA} and *CD11c*^{IRF4} mice. We found that after 14 days, OVA-specific lung CD8$^+$T cells were severely reduced in *XCR1*^{DTA} but not in *CD11c*^{IRF4} mice (Fig.5C-D and S7C-D). By contrast, only TIM3$^+$

517 T_{RM}-like were significantly decreased among Tet$^-$OVA$^+$ CD8$^+$ TILs in *CD11c^{IRF4}* mice,
518 evidencing a differential regulation of T_{RM}-like compared to other CD8$^+$ TILs in antigen-
519 specific context as well. Similar conclusions were obtained using an alternative model of
520 DC2 depletion: DT-treated *Mgl2^{DTR}* mice displayed reduced T_{RM}-like among Tet$^-$OVA$^+$
521 CD8$^+$ TILs while other populations were not significantly impacted (Fig5E-F). In addition,
522 we found that both *XCR1^{DTA}* and *CD11c^{IRF4}* mice had reduced T_{RM}-like among Tet$^-$OVA$^+$
523 CD8$^+$ TILs when engrafted with AT3-OVA tumors.

524 In sum, we have shown above that both migratory DC subsets promote pre-T_{RM}
525 generation in tdLN (Fig.4E-O). To assess the contribution of this tdLN-localized
526 phenomenon on lung T_{RM}-like accrual, we adoptively transferred total CD45.1$^+$ tdLN cell
527 suspensions into KP-bearing CD45.2$^+$ recipient mice (Fig.S7L). Tumor-draining but not
528 unrelated LNs gave rise to T_{RM}-like TILs in KP recipient mice (Fig.S7M-P). We conclude
529 that this system is relevant to test the differentiation potential of activated T cells acting
530 as T_{RM}-like progenitors. We therefore transferred tdLNs from WT, *XCR1^{DTA}* or *CD11c^{IRF4}*
531 CD45.2$^+$ mice to KP-bearing WT CD45.1$^+$ host mice (Fig.5G). This setting allowed us to
532 normalise the lung tumor-microenvironment in recipient mice. Indeed, we observed
533 similar responses in endogenous CD45.1$^+$ CD8$^+$ T cells (Fig.S7Q-R). As anticipated, total
534 donor CD8$^+$T cells from *XCR1^{DTA}* but not *CD11c^{IRF4}* tdLNs were decreased in host lungs
535 7 days post-transfer (Fig.5H-I). However, the generation of T_{RM}-like TILs was impaired
536 when tdLN progenitors originated from *XCR1^{DTA}* or *CD11c^{IRF4}* tdLNs. This finding further
537 substantiates the relevance of CD103$^+$CXCR6$^+$ tdLN cells as progenitors of T_{RM}-like
538 infiltrating tumors.

These results demonstrate that T_{RM}-like TILs activation requires the presence of both migratory DC1s and migratory DC2s in tdLN. By contrast, the generation of non-T_{RM}-like, exhausted $CD8^+$ T cells or $PD1^-$ $CD8^+$ T cell effector populations is more selectively dependent on DC1s and less impacted by DC2 deficiency.

Figure 5 - Efficient generation of T_{RM}-like TILs requires both DC1s and DC2s at the level of tdLN

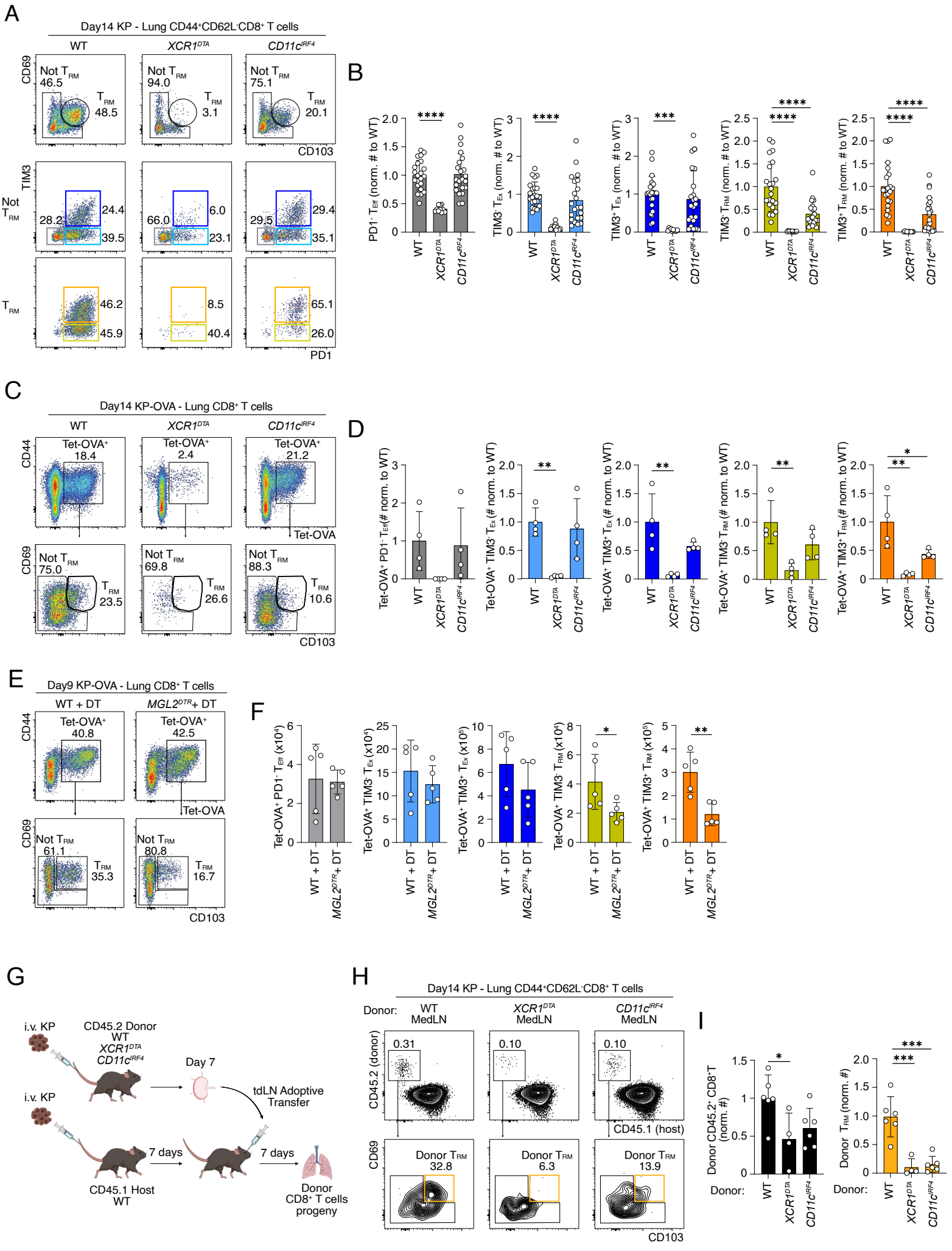

Fig. 5. Efficient generation of T_{RM}-like TILs requires both DC1s and DC2s at the level of tumor-draining lymph nodes.

(**A-B**) Representative flow cytometry plots (A) and quantifications (B) of lung $CD8^+$ T cell populations in WT, *XCR1*^{DTA} or *CD11c*^{IRF4} mice bearing KP-tumors (n = 22 WT, n = 10 *XCR1*^{DTA} and n = 22 *CD11c*^{IRF4} mice, one-way ANOVA tests).

(**C-D**) Representative flow cytometry plots (C) and quantifications (D) of lung tetramer-OVA^+ $CD8^+$ T cell populations in WT, *XCR1*^{DTA} or *CD11c*^{IRF4} mice bearing KP-OVA tumors (n = 4 mice per group, one-way ANOVA tests).

(**E-F**) Representative flow cytometry plots (E) and quantifications (F) of lung tetramer-OVA^+ $CD8^+$ T cell populations in WT or *Mgl2*^{DTR} mice bearing KP-OVA tumors and treated with diphteria toxin as described in Figure 4M (n = 3 WT + DT and n = 5 *Mgl2*^{DTR} + DT mice, unpaired t-tests).

(**G**) Experimental design for the adoptive transfer of total tdLN. Donor $CD45.2^+$ mice (WT, *XCR1*^{DTA} or *CD11c*^{IRF4}) and host $CD45.1^+$ mice were injected with KP cells. 7 days later, total donor tdLN were transferred intravenously in host mice. Lungs from host mice were analyzed 7 days post-transfer.

(**H-I**) Representative flow cytometry plots (H) and quantifications (I) of donor $CD45.2^+$ total $CD8^+$T cells and donor $CD45.2^+$ T_{RM} in the lungs of host $CD45.1^+$ mice bearing KP tumors 7 days post-transfer of WT, *XCR1*^{DTA} or *CD11c*^{IRF4} tdLN (n = 6 WT, n = 4 *XCR1*^{DTA} and n = 6 *CD11c*^{IRF4} donor mice, one-way ANOVA test).

Low TCR triggering by migratory crosspriming DC2s favors CD103 expression while migratory DC1-derived IL-12 supports CXCR6 expression.

Because both types of migratory DCs were required for T_{RM}-specification in tdLN, we wondered which could be the mechanism accounting for their respective contribution. We noticed that both migratory DC1 and DC2 (but not resident DCs) had uptaken tumor-associated antigens, although migratory DC1 were more able to transport tumor antigens to the tdLN (Fig.6A). Migratory DC1 expressed much higher levels of IL-12 (78.3%) than migratory DC2 (15.9%) in IL-12^{YFP} reporter mice (Fig.6B) consistent with higher *Il12b* expression in scRNAseq cluster 8 (Fig.S8A). We found that both migratory DC1 and DC2 cross-presented tumor-associated OVA antigen, although DC1s did it more efficiently than DC2s (319.8 vs 132.8 MFI $H2K^b$-OVA) (Fig.6C). Of note, no signal was detected on resident DCs. Functionally, we evaluated the cross-presentation ability of migratory or resident DCs sorted from KP-OVA tdLNs by co-cultivating them with Cell trace violet (CTV)-loaded OVA-specific OT-1 $CD8^+$ T cells. Migratory but not resident DCs were able to induce OT-1 proliferation and CD44 upregulation (66.4% vs 2.82% of $CTV^{low}CD44^+$) (Fig.S8B). *Ex vivo* addition of synthetic peptide demonstrated that resident DCs are competent in driving OT-1 proliferation when loaded with antigens (Fig.S8C-D). We thus focused our study on migratory DC subsets only. FACS-sorted migratory DC1s and DC2s from KP-OVA-bearing tdLNs (hereafter respectively called, DC1 KP-OVA and DC2 KP-OVA) were co-cultured with CTV-loaded OT-1 for 2 days (Fig.6D). We found that DC1 KP-OVA induced a vigorous proliferation of OT-1 that were almost entirely $CD103^-$ while they expressed homogenously the CD44 activation marker (Fig.6E-F). By contrast,

activation by DC2 KP-OVA was milder but CD44$^+$ proliferating OT-1 expressed high levels of CD103. Addition of DC2 KP-OVA to DC1 KP-OVA OT-1 co-culture did not increase proliferation but promoted CD103 expression on proliferating OT-1 (Fig.6G-H). This demonstrates that DC1s are the main antigen presenting cells and DC2s provide factors upregulating CD103 expression. In a setting where DC1 KP-OVA were too few for efficient OT-1 priming, addition of large numbers of DC2 KP-OVA restored OT-1 proliferation (Fig.S8E-G). Surprisingly, addition of large numbers of DC2 KP with low numbers of DC1 KP-OVA also sustained efficient OT-1 proliferation, as well as strong CD103 expression (Fig.S8E-G). Taken together, these *ex vivo* cross-presentation assays show that the priming of OT-1 is mainly DC1-dependent and that DC2 can promote CD103 expression in an antigen-independent fashion (Fig.S8E-G).

We next wondered which factor could explain the differential ability of DC2s to promote CD103 expression. We showed that IL-12 was highly produced by migratory DC1 (Fig.6B) and IL-12 silences TGF-β activated CD103 expression via TBET competition at SMAD binding elements within CD103 promoter[56]. Therefore, we tested the role of IL-12 *ex vivo* and found that addition of recombinant IL-12 blunted CD103 expression without affecting the proliferation of naïve OT-1 by DC2s KP-OVA (Fig.6E-F). By contrast, IL12 blockade during DC1-dependent activation did not restore CD103 on proliferating T cells. We therefore reasoned that another parameter, distinct from IL-12, was associated to cross-priming by DC1s and limited CD103 expression in activated T cells. We hypothesized that higher levels of MHCI-peptide complexes on DC1s (Fig.6C) could intrinsically limit CD103 expression on activated T cells. To test this, we loaded DC2 KP with increasing

amounts of SIINFEKL synthetic OVA peptide *ex vivo* in the presence of naïve OT1s. We found that peptide add-back was sufficient to impair CD103 expression in $CD44^{+}CTV^{low}$ OT-1 T cells while it increased proliferative expansion, thereby mimicking T cell activation by DC1s (Fig.6I and S8H). We next addressed the role of TCR avidity for MHCI-peptide complexes in controlling CD103 persistence on activated T cells. To this end, we primed naïve OT1s with various altered peptide ligands acting as weaker agonists for the OT1 TCR[57]. We observed a decrease of OT-1 activation with low affinity peptides (SIINFEKL>Q4>T4>G4), associated to an increased expression of CD103 on $CD44^{+}$ divided OT-1 cells (Fig.6J and S8I). Overall, we conclude that a mild TCR triggering and low levels of IL-12 are both required for the persistence of CD103 on T cells during their cross-priming by migratory DCs. However, CXCR6 expression is also a hallmark of early-activated pre-T_{RM}-like in tdLNs (Fig.3). We found that IL-12 blockade *in vivo* blunted T cell activation while inhibiting CXCR6 expression in tdLNs (Fig.6K-M and S8J). Consistently, IL-12 also promoted CXCR6 expression during the priming of naïve OT1 *in vitro* (Fig.6N-O). This shows that IL-12, despite its inhibitory effect on CD103, is required to acquire the pre-T_{RM}-like phenotype. Given the paramount role of TGF-β signaling in the specification of T_{RM}[58], we further tested the role of IL-12 in combination with TGF-β *in vitro*. We found that IL-12 inhibited TGF-β signaling supporting CD103 expression (Fig.6N-O). Vice versa, TGF-β counteracted i) TCR-induced CD103 inhibition and ii) IL-12-induced CXCR6 expression (Fig.6N-O). As a result, optimal generation of $CD103^{+}CXCR6^{+}$ OT1s required both IL-12 and TGF-β and intermediate levels of antigen presentation ensuring mild TCR triggering (Fig.6N-O). Consistently, both migratory DC1 and migratory DC2 expressed αV-β8 and GARP TGF-β presentation molecules, but migratory DC2 displayed

significantly higher membrane LAP expression, showing a superior pro-TGF-β production (Fig.S8K-M).

Altogether, we conclude that ***i***) both migratory DC1 and migratory DC2, (but not resident DCs) cross-present KP-associated antigens to T cells in tdLNs. ***ii***) DC1s are the most efficient at antigen uptake, cross-presentation and in triggering $CD8^+$ T cell proliferative expansion concomitant with the loss of CD103 which is dependent on both efficient TCR triggering and IL-12 release. ***iii***) IL-12 low DC2s are inefficient at uptake, cross-presentation and in triggering $CD8^+$ T cell proliferative expansion but the low efficiency of antigen cross-presentation by migratory DC2s is required for CD103 persistence on $CD44^+$ activated T cells by delivering a milder TCR signalling as compared to DC1s. ***iv***) despite its inhibitory effect on CD103 expression, IL-12 is crucially needed for CXCR6 expression.

Figure 6 - Low TCR triggering by migratory crosspriming DC2s favors CD103 expression while migratory DC1-derived IL-12 supports CXCR6 expression

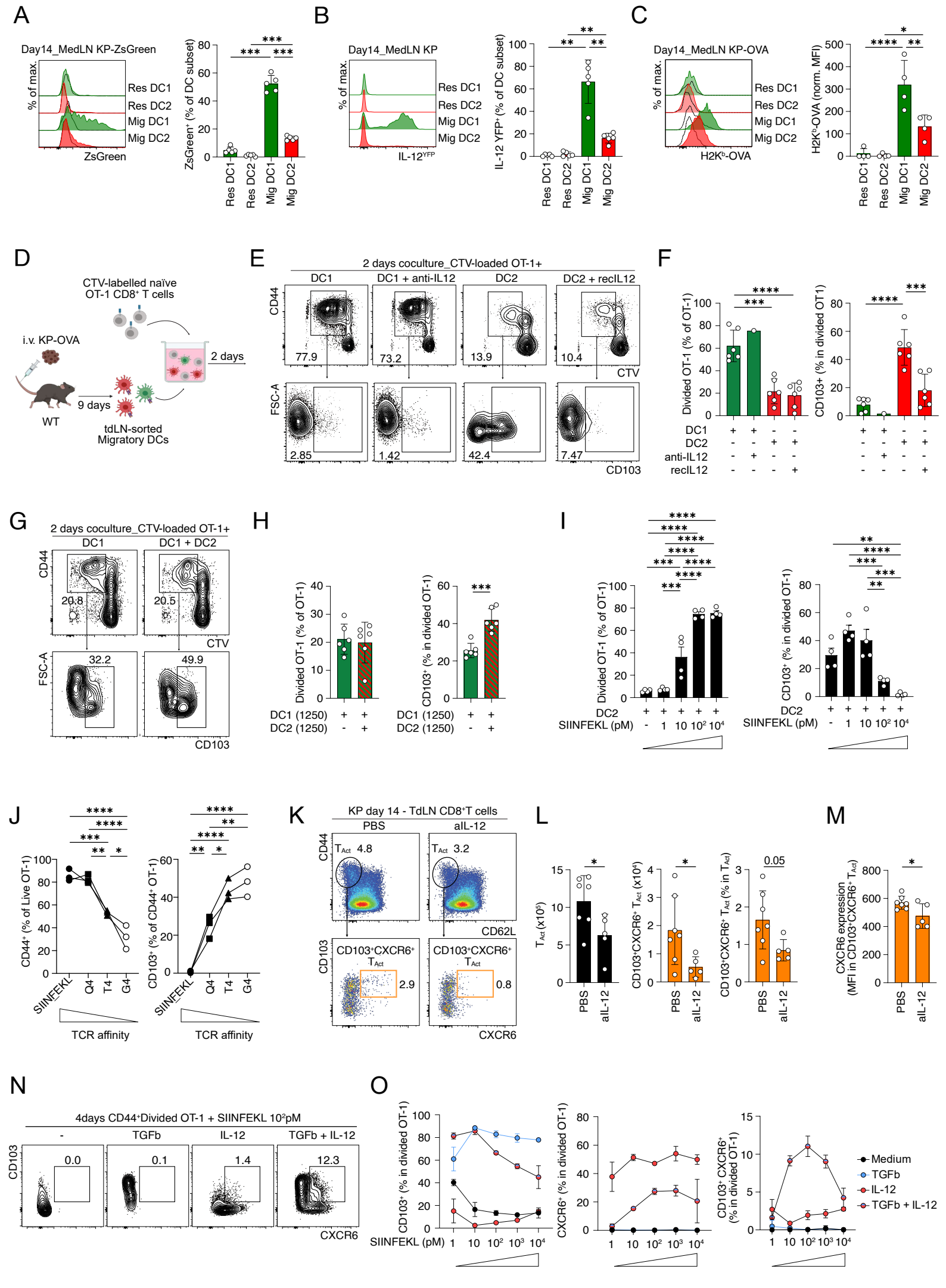

Fig. 6. Low TCR triggering by migratory crosspriming DC2s favors CD103 expression while migratory DC1-derived IL-12 supports CXCR6 expression.

(**A**) Representative flow cytometry plot and quantification of ZsGreen^{+} resident and migratory DC1 and DC2 in tdLN of mice bearing KP-ZsGreen tumors (full line) (n = 5 mice, one-way ANOVA tests). Dotted lines represent control KP-injected mice for each subset.

(**B**) Representative flow cytometry plot and quantification of IL-12-YFP^{+} resident and migratory DC1 and DC2 in tdLN of IL-12^{YFP} mice bearing KP tumors (n = 5 mice, one-way ANOVA tests).

(**C**) Representative flow cytometry plot and quantification of H2K^{b}-OVA expression on resident and migratory DC1 and DC2 in tdLN of mice bearing KP-OVA tumors (full line). H2Kb-OVA MFI were normalized with KP-injected mice (dotted line).

(**D**) Experimental design for the *ex vivo* cocultures. Migratory DC subsets were FACS-sorted from tdLN of mice bearing KP-OVA tumors at day 9 and cocultured with CTV-loaded naïve OT-1 cells for 2 days.

(**E-F**) Representative flow cytometry plots (E) and quantifications (F) of CTV-loaded naïve OT-1 cells cultured for 2 days with flow cytometry-sorted migratory cDC1 or migratory DC2 from tdLN of mice bearing KP-OVA tumors in presence or not of recombinant IL-12p70 or anti-IL-12p40 neutralizing antibody.

(**G-H**) Representative flow cytometry plots (G) and quantifications (H) of CTV-loaded naïve OT-1 cells cultured for 2 days with 1250 migratory cDC1 alone or together with 1250 migratory DC2 sorted from tdLN of mice bearing KP-OVA tumors.

667 (**I**) CTV-loaded OT-1 cells were cultured for 2 days with flow cytometry-sorted migratory
668 DC2 from tdLN of mice bearing KP tumors in presence of increasing SIINFEKL peptide
669 concentration (1pM, 10pM, 10^2pM and 10^4pM). Divided OT-1 and CD103 expression
670 were quantified (n = 4 mice, paired one-way anova tests). See also Figure S8H.
671 (**J**) Naïve OT-1 cells were cultured for 4 days with SIINFEKL peptide and low affinity
672 peptides SIIQFEKL (Q4), SIITFEKL (T4) and SIIGFEKL (G4) at 10^2pM. $CD44^+$ activated
673 OT1 and CD103 expression were quantified (n = 3 replicates, paired one-way anova
674 tests). See also Figure S8I.
675 (**K-M**) Mice were injected i.v. with KP tumors and treated with anti-IL-12p40 neutralizing
676 antibody every 3 days from day 0 to 14 as depicted in figure S8J. Representative flow
677 cytometry plots (K) and quantifications of T_{Act}, $CD103^+CXCR6^+$ T_{Act} (L) and CXCR6
678 median fluorescence intensity within $CD103^+CXCR6^+$ T_{Act} (M) (n = 7 control and n = 5
679 anti-IL12 treated mice, unpaired t-tests).
680 (**N-O**) Representative flow cytometry plots (N) and quantifications (O) of CTV-loaded OT-
681 1 cells cultured for 4 days in the presence of increasing SIINFEKL peptide concentrations
682 (1pM, 10pM, 10^2pM, 10^3pM and 10^4pM) and cytokines TGF-β, IL-12 or both (n = 3
683 replicates). CD103 and CXCR6 expression were analyzed.

Cross-priming by migratory DC2s recapitulates the T_{RM} transcriptional program.

We next sought to analyse how the identity of migratory DCs subset controlled the transcriptional phenotype of $CD8^+$ T cells during cross-priming. To this end, we performed bulk RNAseq on OT1 cells that did or did not upregulate CD103 after *ex vivo* crosspriming by migratory DC1 or DC2 sorted from tdLN of KP-OVA bearing mice (Fig.7A). PCA analysis revealed a stronger segregation between DC1 and DC2-activated OT1 across PC1 (84% of the variance) compared to CD103 expression (Fig.7B). We conclude that the identity of migratory DCs cross-priming T cells is the main factor driving their transcriptional phenotype. PC1 was positively driven by T_{RM}-associated genes (*Itgae*, *Cd226 e.g.*) and stemness genes (*Klf2, Sell, Slamf6, Il7r, e.g.*) and negatively driven by effector-related genes (*Il12rb1 and Il12rb2, Tbx21, Gzmb, Eomes, e.g.*) and proliferation associated transcription factor *Myc*. T_{RM}-associated signatures found in tdLNs pre-T_{RM}s (by scRNASeq, DEG Cluster 8 *Cxcr6*$^+$ or bulk RNA-Seq, $CD103^+$ T_{Act} > $CD103^-$ T_{Act}) or lung T_{RM}-like TILs (bulk RNA-Seq, $TIM3^+$ T_{RM} >$TIM3^+$ T_{Exh}) associated primarily with $CD103^+$ OT1 crossprimed by DC2s ($CD103^+$ $OT1_{DC2\text{-}Act}$, Fig.7C). By contrast, signature of genes downregulated in pre-T_{RM} (bulk RNA-Seq, $CD103^-$ T_{Act} > $CD103^+$ T_{Act}) was poorly expressed by $CD103^+$ $OT1_{DC2\text{-}Act}$. GSEA analysis of $CD103^+$ $OT1_{DC2\text{-}Act}$ compared to all other OT1 populations, hereafter referred as Rest, further confirmed these results (Fig.7D). $CD103^+$ $OT1_{DC2\text{-}Act}$ were enriched in T_{RM}-associated genes *Itgae*, *Cd226*, *Cxcr6* or *Inpp4b*, stemness-related genes *Il7r and Tcf7* and TGF-β receptor genes *Tgfbr1* and *Tgfbr2* (Fig.6E). Conversely, $CD103^+$ $OT1_{DC2\text{-}Act}$ expressed lower levels of effector-related genes *Gzmb*, *Klrk1*, *Eomes* or *Tbx21*, proliferation-associated transcription factor *Myc*

706 and Il12r genes *Il12rb1* and *Il12rb2* (Fig. 7E). Consistently, GSEA scoring of a memory
707 CD8 T cell signature revealed that CD103^{+} OT1$_{DC2\text{-}Act}$ had increased expression of
708 memory-related genes (NES = 1.46, Fig.7F). We also evaluated a signature of SMAD4
709 target genes, a central mediator of TGF-β signalling, and found that it was enriched in
710 CD103^{+} OT1$_{DC2\text{-}Act}$ (NES = 1.32, Fig.7F). Conversely, MTORC1 signaling (NES = -1.58)
711 and MYC targets (NES = -1.57) signatures were strongly reduced in CD103^{+} OT1$_{DC2\text{-}Act}$,
712 consistent with reduced proliferation activity (Fig.7G).

713 Taken together, these results indicate that migratory DC2s recapitulate the differentiation
714 of naïve OT1s into pre-T_{RM}-like similar to those found in tdLNs of tumor-bearing mice.
715 The specification of T_{RM} program within naïve T cells is enabled by a stronger activation
716 of TGF-β signalling pathway by migratory DC2s as compared to migratory DC1s.

Figure 7 - Crosspriming by migratory DC2s recapitulates the T_{RM} transcriptional program

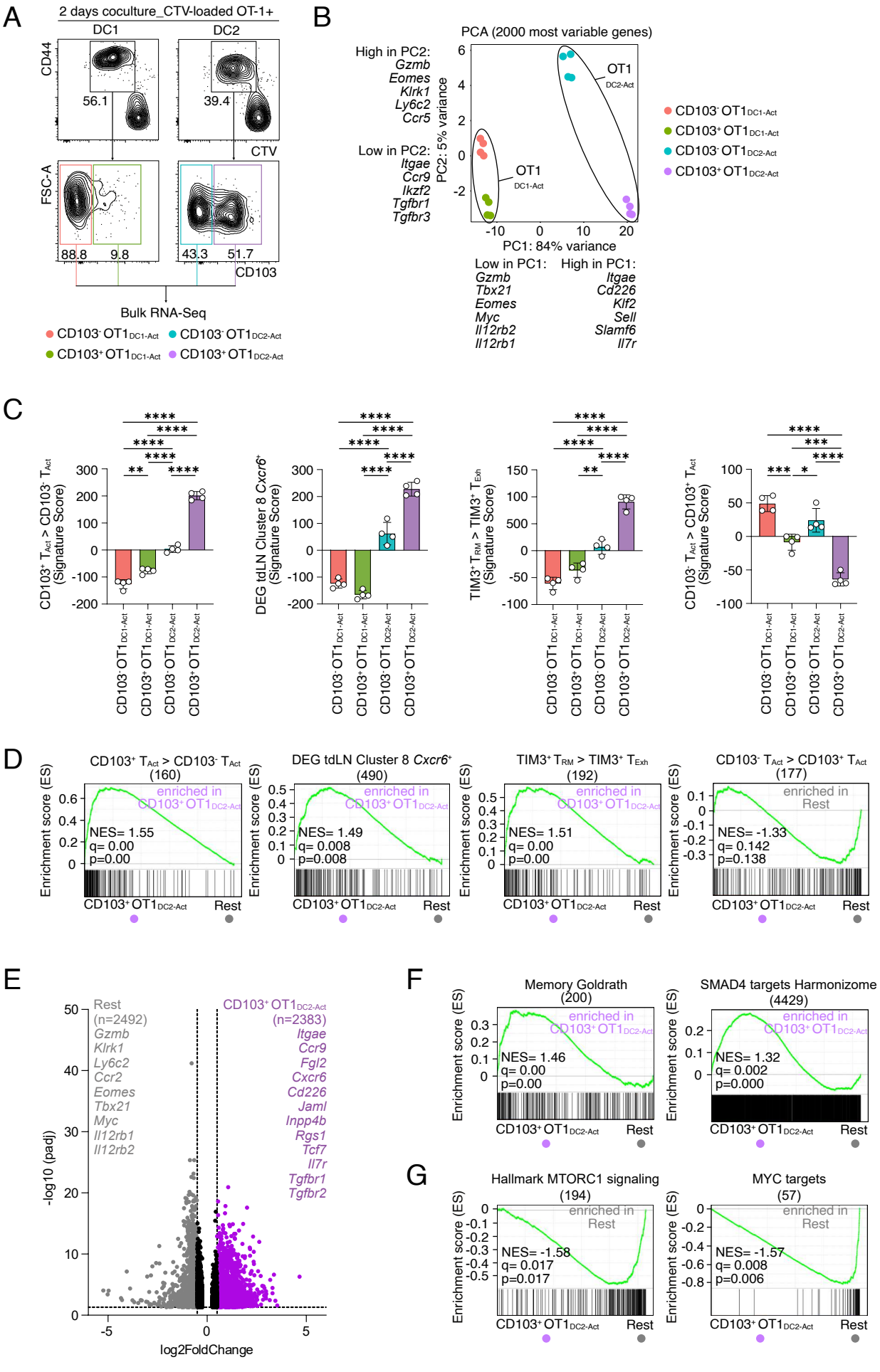

Fig. 7. Crosspriming by migratory DC2s recapitulates the T_{RM} transcriptional program.

(**A**) CTV-loaded naïve OT-1 cells were cultured for 2 days with flow cytometry-sorted migratory DC1 or migratory DC2 from tdLN of mice bearing KP-OVA tumors. $CD103^+$ and $CD103^-$ divided OT1 activated by DC1 or DC2 were FACS-sorted and bulk-RNA sequencing was performed.

(**B**) Principal-component analysis (PCA). Top high and low loading genes are indicated for PC1 and PC2.

(**C**) Scoring of previously defined gene signatures for tdLN $CD103^+$ T_{Act} (bulk RNA-seq), tdLN Cluster 8 *Cxcr6*$^+$ (scRNA-seq), lung T_{RM}-like TILs (bulk RNA-Seq) and tdLN $CD103^-$ T_{Act} (bulk RNA-seq).

(**D**) GSEA of pairwise comparisons of $CD103^+$ $OT1_{DC2\text{-}Act}$ vs all other OT1 populations (termed as Rest) for gene signatures of tdLN $CD103^+$ T_{Act} (bulk RNA-seq), tdLN Cluster 8 *Cxcr6*$^+$ (scRNA-seq), lung T_{RM}-like TILs (bulk RNA-Seq) and tdLN $CD103^-$ T_{Act} (bulk RNA-seq).

(**E**) Volcano plot representing differentially expressed genes (DEGs) between $CD103^+$ $OT1_{DC2\text{-}Act}$ and all other OT1 populations (Rest). Genes with a Log2(fold change, FC) > ±2 and a false discovery rate (FDR)-adjusted p-value of less than 0.05 were considered significant.

(**F-G**) GSEA of pairwise comparisons of $CD103^+$ $OT1_{DC2\text{-}Act}$ vs all other OT1 populations (Rest) for gene signatures of memory CD8 T cells[59] and SMAD4 targets [60](**F**) or Hallmark MTORC1 signaling and MYC targets [61](**G**) extracted from the MSigDB website.

DISCUSSION

Infiltration of solid tumors with $CD8^+$ TILs with a T_{RM} phenotype is predictive of improved survival and better response to immunotherapies[1,3,5–9]. Besides, T_{RM}-like TILs show signs of superior anti-tumor activity as compared to other T cell populations[16,17,20,21]. Therefore, we have sought to address the mechanisms governing the acquisition of the T_{RM} phenotype during T cell activation in tumors. Using a combination of transcriptomic and flow cytometry approaches, we identified a population of T_{RM}-like TILs specifically expressing canonical T_{RM} markers and sharing the expression of exhaustion molecules with T_{Ex} TILs. Fate mapping experiments show that CD103 expression during the early phases of T cell activation in tdLNs defines $CD8^+$ T cells committed to generate T_{RM}-like TILs. Previous studies similarly identified CD103 as a marker of T_{RM}-commitment within naïve T cells in a model of skin vaccination[24]. Using unsupervised analysis of activated T cells in the tdLN, we improved this phenotypic characterization and identified a rare population of $CXCR6^+CD103^+$ T_{RM}-like cells. We further addressed the dendritic cell requirements for T_{RM} phenotype specification. Induction of $CD103^+CXCR6^+$ T_{RM}-like precursor cells in tdLNs is dependent on both migratory DC1s and DC2s. Consistently, lung T_{RM}-like TILs accrual requires both types of migratory DCs at the level of tdLN. By contrast, effector and exhausted $CD8^+$ T cells infiltrating tumors solely rely on DC1s. Finally, we asked which factors provided by DCs subsets could control T_{RM}-like TILs generation. We provide evidence that T_{RM} specification in tdLNs:

i) requires sub-optimal TCR triggering by weak cross-presenter DC2s that display reduced densities of MHCI-peptide complexes.

762 *ii)* is inhibited by high amounts of IL-12 mainly produced by DC1s that inhibits
763 TGF-β signalling and its CD103 downstream target.

764 *iii)* necessitates some levels of IL-12 as evidenced by the IL-12 function in
765 upregulating CXCR6 during T cell cross-priming.

766 *iv)* relies on the proliferative expansion uniquely achieved by cross-priming DC1s.

767 **T_{RM} specification occurs in tdLNs and involves both $XCR1^+$ and $CD11b^+$ migratory**
768 **DCs.**

769 The existence of precursors pre-committed to differentiate into T_{RM} has been
770 demonstrated within naïve $CD8^+$ T cells epigenetically poised to express T_{RM}-associated
771 genes[24] and within blood circulating activated T cells after skin vaccination[26]. Mani et al.
772 showed that TGF-β activation by migratory DCs was required for T_{RM} preconditioning at
773 the level of naïve T cells in the LN. Whether this mechanism requires one or multiple DC
774 subsets has not been addressed. Also, it is unknown which DC subset participate to the
775 activation of T_{RM} from T_{RM}-poised naïve progenitors. Our study identifies a subset or early
776 activated $CD8^+$ T cells expressing selectively a transcriptional signature of tumor-
777 infiltrating T_{RM} in tdLN. We demonstrate that the activation of tdLN $CD103^+CXCR6^+$ T
778 cells rely on both migratory DC1s and DC2s. By contrast, activation of $CD103^-$ $CD8^+$ T
779 cells is largely independent on the presence of migratory DC2s. Furthermore, we
780 demonstrate by adoptive transfer that genetically labelled $CD103^+$ T cells from tdLNs
781 uniquely give rise to lung T_{RM}-like TILs. Therefore, we establish that the specification of
782 lung T_{RM}-like TILs actually starts within lymph nodes by a process orchestrated by both
783 migratory DCs subsets.

These findings might have a relevance in humans since CD1c$^+$ DCs have been shown to participate to the activation of CD8$^+$CD103$^+$ T_{RM}-like cells[39,40]. Of note, the contribution of DC2s to the generation of memory but not effector T cell responses had been previously noted in the influenza infection model[38] and to the maintenance of anti-infectious T_{RM} at mucosal sites in HSV infection[27]. Altogether, our results further extend the major contribution of DC1s in anti-tumor CD8 T cell immunity to T_{RM}[29,30,34,53,54]. Our findings are in line with pioneer studies highlighting the crucial role of DC1s in the activation of vaccine-induced T_{RM}s[37]. However, it is important to underline that the role of DC2s had not been addressed in this context. In addition, we evidence a contribution of DC2s to T_{RM} generation at the level of tdLNs.

Low TCR signal strength, IL12 and TGF-β synergize to differentiate T_{RM}

T_{RM} development dependency on TGF-β has been well established in several studies[24,25,27]. However, both migratory DC subsets express TGF-β activating molecules at the transcriptomic level (e.g., *Itgav*)[24]. Therefore, migratory DC2s might contribute to T_{RM} specification i) by providing a milder TCR signal strength because they cross-present tumor associated antigens inefficiently; ii) by not providing IL-12 in contrast to DC1s; iii) by providing specific signals yet to be identified. Here, we provide evidence for i) and ii). We show that sub-optimal cross-presentation by DC2s enable CD8$^+$ T cells to maintain CD103 expression during T cell activation *in vitro*. These results are in line with previous studies highlighting a negative impact of strong TCR signalling on T_{RM} differentiation in vivo in the context of viral infections[62,63]. More recently, Shakiba et al. have shown that low affinity tumor-associated antigens prime T cells expressing higher levels of CD103

806 while presenting less features of dysfunctional/exhausted T cells as compared to T cells
807 primed with high affinity antigens[64]. Finally, both mild TCR signalling[65] and migratory
808 DC2s contribute to the priming of central memory $CD8^+$ T cells[66]. In addition to optimal
809 cross-priming efficiency, migratory DC1s also provide high levels of IL-12 which acts as
810 an inhibitory signal erasing CD103 expression induced by IRF4-dependent migratory
811 DC2s. These findings are in line with the regulatory role of TBET, downstream of IL-12
812 signalling at SMAD3 binding sites in the CD103 locus[56,67]. Bergsbaken et al. have noticed
813 that IL-12 promotes $CD103^-$ but not TGF-β dependent $CD103^+$ T_{RM} by a STAT4-
814 dependent mechanism[68,69]. Our results clearly establish that TGF-β-dependent program
815 is induced more efficiently by migratory DC2s than migratory, IL-12-producing DC1s.
816 TGF-β transpresentation might play a role in this process, together with the regulatory
817 role of IL-12 on TGF-β signalling (that can be visualized by IL-12 ability to counteract
818 TGF-β-induced CD103).

819 **Functional features associated to the T_{RM} phenotype in cancer**

820 T_{RM} have been extensively studied in the context of infections or vaccination when
821 memory is settled and maintained after antigen clearance. In this study, we have not
822 addressed the functional ability of T_{RM}-like cells to recirculate or generate memory.
823 Recent studies addressing the functional ability of T_{RM}-like cells to recirculate in a mouse
824 model of E0771 breast cancer suggest that T_{RM} phenotype does not necessarily correlate
825 with tumor residence or correspond to neo-generated T_{RM}-like cells from circulating
826 precursors[15]. However, T_{RM}-like cells in this model do not express CD103 which may be
827 a major contributor of residence within the tumor through direct interaction with epithelial

828 E-Cadherin which is not expressed in the E0771 cells investigated in this study[70,71].
829 Evaluating this possibility would require additional experiments.

830 From a functional perspective, T_{RM}-like could represent a quiescent pool of responsive
831 cells, able to generate effector cells if recruited by immunotherapies[3,9,20]. This could
832 explain why T_{RM}- and migratory DC2 deficient mice do not exhibit a major deficit in tumor
833 control. However, our experimental analysis of ICB immunotherapy suggest that
834 immunotherapy increases the frequency and functionality of tdLN-associated, tumor-
835 specific pre-T_{RM}-like and their tumor TILs T_{RM}-like progeny. This view is in line with the
836 developmental plasticity of T_{RM} upon antigenic restimulation that had been established in
837 infection-induced T_{RM}s[18,19]. Deeper functional studies are required to understand the
838 determinants of the prognosis value of T_{RM}-like phenotype in cancer and how their
839 functionality could be activated.

840

841 In conclusion, our study highlights the fine-tuning of anti-tumor $CD8^+$ T cell diversity by
842 multiple migratory DCs subsets in tdLNs. We show that the crosspriming of $CD8^+$ T cells
843 reaching a dysfunctional/exhausted phenotype within tumors is uniquely dependent on
844 DC1s and entirely independent on migratory DC2s. By contrast, induction of T_{RM}-like cells
845 requires both DC1 and DC2 subsets. These findings challenge the relevance of the
846 “division of labor” across DCs subsets ascribing discrete, specific and exclusive immune
847 functions to specific DCs subsets. Instead, we evidence a high level of cooperativity
848 relevant for the induction of memory precursors in tumor-draining lymph nodes. In sum,

849 our findings support the view that instruction of residency program and proliferative
850 expansion rely on complementary yet distinct DCs subsets.

851 These findings have important implications for the design of effective immunotherapies
852 harnessing multiple types of $CD8^+$ T cell immunity, *id est* effector vs tissue-resident
853 memory cells. One correlates of the current findings that remain to be tested, is that
854 optimal priming of diverse T cell phenotypes might rely on antigen delivery to multiple
855 DCs subsets.

METHODS

Study design

The aim of this study was to understand the dendritic cells requirements for T_{RM} specification in lung cancer. To that end, we intravenously injected KP lung tumors into several mouse models in which specific dendritic cell populations can be manipulated. We thoroughly characterized polyclonal and antigen-specific CD8 T cell populations to model antigen OVA using a combination of transcriptomics (bulk RNA-seq, scRNA-seq, CITE-Seq) and flow cytometry approaches. To address the role of dendritic cells in the lymph nodes, we designed a series of adoptive cell transfer and *ex vivo* OT1-dendritic cell coculture experiments.

Mice

Mice were housed at the INSERM U1149 CRI, Medicine school site Bichat or at the Paris Institut Pasteur animal house facilities. Wild type C57BL/6J and CD45.1 mice were purchased from Janvier and kept in our facility. *XCR1*^{cre} and Rosa26-lox-stop-lox-DTA (B6.129P2 Gt(ROSA)26Sortm1(DTA)Lky/J)[72] mice were kindly provided by Dr. Marc Dalod (Center of Immunology Marseille-Luminy, Marseille). XCR1^{DTA} mice were generated as described[51]. OT-1 *RAG2*$^{-/-}$ CD45.1 mice were kindly provided by Dr. Sébastian Amigorena (Curie institute, Paris). *Flt3L*$^{-/-}$ and *Zbtb46*^{cre} (B6.Cg-*Zbtb46*$^{tm3.1(cre)Mnz}$/J) mice[48] were kindly provided by Dr. Guillaume Darrasse-Jèze (UMR-S 979, Paris). *CD11c*^{cre} mice (B6.Cg-Tg(Itgax-cre)1-1Reiz/J;[73]), *IRF4*^{flox} mice (B6.129S1-Irf4tm1Rdf/J;[74]), and *CCR2*$^{-/-}$ mice (Ccr2tm1/fc;[75]) were kindly gifted by Dr. Emmanuel Gautier (UMR-S U1166, Paris). Hobit-tdTomato-DTR [B6-Tg (Zfp683-tdTomato-P2A-

878 Cre-P2A-DTR);[18]] mice were kindly provided by Dr. Klaas Van Gisbergen,
879 (Champalimaud Fundation, Lisbon). The reporter/deleter cassette disrupts the Hobit
880 allele, in consequence, heterozygous Hobit tdTomato-DTR mice were used in the
881 experiments. *KRAS*$^{LSL\text{-}G12D/+}$*;p53*$^{fl/fl}$ mice[76] were kindly provided by Dr. Kairbaan
882 Hodilvala-Dilke (Bart Institute Queen Mary University, London). CD103$^{cre\text{-}ERT2}$ (*Itgae*-
883 creER^{T2}) and Rosa$^{LSL\text{-}tdTomato}$ (B6.Cg-*Gt(ROSA)26Sor*$^{tm14(CAG\text{-}tdTomato)Hze}$/J) mice were
884 kindly provided by Dr. Tessa Bergsbaken (Rutgers, New Brunswick)[45]. IL-12^{YFP}
885 (C.129S4(B6)-Il12btm1.1Lky/J;[77]) mice were kindly provided by Dr. Mikaël Pittet
886 (University of Geneva). *Mgl2*^{DTR} (B6(FVB)-*Mgl2*$^{tm1.1(HBEGF/EGFP)Aiwsk}$/J) mice[55] were kindly
887 provided by Dr. Yosuke Kumamoto (Rutgers, New Jersey). *Ms4a3*^{cre} (C57BL/6J-
888 *Ms4a3*$^{em2(cre)Fgnx}$/J) mice[78] were kindly provided by Dr. Camille Bleriot (Institut Gustave
889 Roussy, Paris) and Dr. Florent Ginhoux (Institut Gustave Roussy, Paris). *Lyz2*^{cre}
890 (B6.129P2-*Lyz2*$^{tm1(cre)Ifo}$/J) mice[79] were kindly provided by Dr. Loredana Saveanu
891 (INSERM U1149, Paris). The study was approved by the local ethics committee comité
892 d'éthique Paris Nord no. 121 and the Ministère de l'enseignement supérieur, de la
893 recherche et de l'innovation under the authorization number APAFIS#15373. Animal care
894 and treatment were conducted with national and international laws and policies
895 (European Economic Community Council Directive 86/609; OJL 358; December 12,
896 1987). All experiments were performed in accordance with the Federation of European
897 Laboratory Animal Science Association (FELASA) guidelines institutional guidelines and
898 the French law.

899 **Tumor cell lines**

The KP line has been isolated from primary lung tumors of C57BL/6 KP mice (*KRAS*$^{LSL\text{-}G12D/+}$;*p53*$^{fl/fl}$)[80]. The line was kindly provided by Dr. Federica Benvenuti (ICGEB, Trieste), and has been used previously[35,81]. KP-OVA were generated by retroviral transduction of KP cells with a pBabe-OVA-IRES-Cherry vector. KP-ZsGreen were generated by lentiviral transduction of KP cells with a pLVX-IRES-ZsGreen vector. Tumor cell lines were cultured in RPMI 1640 medium, Glutamax (Thermo Fisher) supplemented with 10% fetal bovine serum (FBS) (Thermo Fisher), penicillin-streptomycin (Thermo Fisher) and 55µM β-mercaptoethanol (Thermo Fisher) (complete RPMI) and maintained at 37°C and 5% CO2. The AT3-OVA line was kindly provided by Dr. Julie Helft (Institut Cochin, Paris).

Tumor models

For the grafted KP tumor models, the KP, KP-OVA and KP-ZsGreen tumor cell lines were grown in RPMI-Glutamax with 10% FCS, 55 µM 2-mercaptoethanol, Penicillin streptomycine and used for experiments when in exponential growth phase. The cells were detached using Trypsine/EDTA 0.25%, washed two times in PBS and counted in trypan blue. 8.10^5 tumor cells were intravenously injected in 100 µL RPMI without supplement.

For the autochthonous KP model, C57BL/6 KP mice (*KRAS*$^{LSL\text{-}G12D/+}$;*p53*$^{fl/fl}$) at 8 weeks of age, were intranasally inoculated with 2.5×10^7 infectious particles of a replication-deficient adenoviral vector with Cytomegalovirus promoter driving the expression of the Cre recombinase protein in order to sporadically induce mutations in lung cells, and promote lung tumor development as previously described[62]. Mice were sacrificed 16 weeks after the adenovirus inoculation.

For the AT3-OVA orthotopic tumor model, cells were grown in RPMI-Glutamax with 10% FCS, 55 µM 2-mercaptoethanol, Penicillin streptomycine and used for experiments when in exponential growth phase. The cells were detached using Trypsine/EDTA 0.25%, washed two times in PBS and counted in trypan blue. 5.10^5 tumor cells were injected orthotopically in the mammary gland in 100 µL RPMI without supplement. Tumor dimensions were recorded every 2-3 days using a digital caliper, and tumor volume (V) was calculated using the formula V=(L×W×W)/2, with volume expressed in mm^3. Mice were monitored daily, and endpoints were established based on signs of distress, including pain, lethargy, dehydration, ulceration, or tumor necrosis. Mice were sacrificed when these criteria were met or when tumor volume reached 1500 mm^3.

***In vivo* treatments**

For the FTY treatment, mice received intraperitoneal injections of 1 mg/kg FTY720 (fingolimod) (Sigma-Aldrich) in 150 µl of non-deionised H_20 (Versol) every 3 days from day 1 after tumor injection.

For IL-12p40 blocking, mice received intraperitoneal injections of 200µg anti-IL-12p40 blocking antibody (Biolegend) in 200µl of PBS every 3 days from day 0 after tumor injection.

For chronic ICB immunotherapies, mice received intraperitoneal injections of 200µg control isotype (clone 2A3, BioXCell BE0089), anti-CTLA-4 (clone 9H10, BioXCell BE0131), anti-PD-1 (clone 29F.1A12, BioxCell BE0273) or both anti-PD-1 and anti-CTLA-4 antibodies in 200µl of PBS every 3 days from day 7 after KP-OVA tumor injection and mice were sacrificed at day 17 for T cell analysis.

For acute ICB immunotherapy, mice received one intraperitoneal injection of 200µg anti-PD-1 antibody at day 14 post-tumor injection and mice were sacrificed 2 days later (day 16).

For diphteria toxin (DT) treatments, *Mgl2*^{DTR} mice were injected intraperitoneally with PBS or 700ng DT (Sigma D0564) in 200µl of PBS at day 8 post-KP tumor injection and depletion efficiency was assessed one day later (day 9). For chronic depletion, WT or *Mgl2*^{DTR} mice were injected with DT at days 2, 5 and 7 post-KP-OVA tumor injection and T cells were analyzed at day 9.

Mouse tissues processing

Mouse lungs were harvested and transferred to 3ml digestion buffer (Hank's Balanced Salt Solution (HBSS) with calcium and magnesium (Thermo Fisher) and with 75 µg/mL of Liberase TL (Roche) and 0.02mg/ml DNase I (Thermo Fisher)). Lungs were dissociated using gentleMACS Octo Dissociator (Miltenyi) (program m_lung_01), incubated at 37°C for 45 minutes and dissociated again on the gentleMACS Octo Dissociator (Miltenyi) (program m_lung_02). AT3-OVA tumors were harvested, mechanically dissociated and similarly digested. The cell suspensions were passed through 70 µm cell strainers (Corning) and red blood cells were lysed using ACK lysing buffer (Thermo Fischer). The mediastinal lymph nodes were smashed in FACS buffer on a 70 µm cell strainer. The absolute number of live immune cells in each tissue cell suspension was assessed using AccuCheck Counting Beads (Thermo Fisher) along with anti-CD45 and DAPI staining on BD FACS Fortessa 20 (BD Biosciences). For OT-1 CD8^{+}T cell preparation, LNs from OT-1 CD45.1 RAG mice were passed through 70 µm cell strainers. The LN suspensions were

stained with anti-CD8-APCCy7 and counted by FACS using counting beads (AccuCheck beads, Invitrogen).

Flow cytometry analysis

After tissue processing and cell counting, Fc-receptor were blocked using FcBlock (2.4G2, BD) for 15min at 4°C. For dead cell identification, the cells were stained with 7-AAD (Biolegend) for extracellular staining only or Zombie dye (Biolegend) for intracellular staining in PBS. Cells were then stained with fluorophore-conjugated antibodies in FACS buffer (See antibody list in the Key resource table), PBS 3% FCS (Gibco) 2mM EDTA (Gibco), during 30 minutes at 4°C. When needed, cell suspensions were subsequently fixed and stained in for nuclear protein (30min fixation and 30min intracellular staining) using fixation/permeabilization kit (eBiosciences transcription factor staining buffer) according to the manufacturer's instructions. Labelling with $H2K^b$-SIINFEKL tetramers (MBL) was performed at room temperature for 30 min. Data acquisition was performed using an LSR-Fortessa X20 (BD) and analysis were done using FlowJo software (TreeStar).

***Ex vivo* T cell restimulation assay**

After tissue processing and cell counting, 1 million total $CD45^+$ cells were incubated for 5 hours at 37°C in a restimulation cocktail composed of 50ng/ml PMA (Sigma), 1µg/ml Ionomycin (Sigma), 2µg/ml Golgi Plug (BD) and 2µg/ml Golgi stop (BD) in complete RPMI medium. Cells were then processed for flow cytometry analysis as described before.

***Ex vivo* tumor-T cell coculture assay**

1000 KP-OVA tumor cells were seeded in 96 well plates. One day later, 3000 PD1$^+$ T_{Ex} or 3000 PD1$^+$ T_{RM}-like were sorted from the lungs of KP-OVA bearing mice at day 14 and cocultured for 4 days with KP-OVA tumors cells in complete RPMI medium. 4 days later, supernatants were harvested for ELISA quantification of IFNγ (Biolegend 430804) and Granzyme B (R&D DY1865). T cells were harvested and KP-OVA tumor cells were detached using Trypsin/EDTA 0.25% and counted by FACS.

Bulk RNA-sequencing

After tissue processing and cell count, cell suspensions were washed in cold FACS buffer (PBS + 3% BSA + 2mM EDTA), Fc-receptors were blocked ,15min at 4°C, using purified anti-CD16/32 (2.4G2) and, then, stained with fluorophore conjugated antibodies for 30 minutes at 4°C. CD8$^+$T cell subsets from tumor-bearing lungs and tdLNs were isolated using an Aria III (BD) and a MELODY (BD) cell sorter, respectively, and directly collected on lysing TCL buffer (QIAGEN) containing 0.1% of beta-mercaptoethanol before storage at -80°C. RNA were extracted and isolated using the Single Cell RNA purification kit (Norgen, Cat#51800) according to the manufacturer's instructions. After extraction, total RNA was analyzed using Agilent RNA 6000 Pico Kit on the Agilent 2100 Bioanalyzer System. RNA quality was estimated based on capillary electrophoresis profiles using the RNA Integrity Number (RIN). RNA sequencing libraries were prepared using the SMARTer Stranded Total RNA-Seq Kit v2 - Pico Input Mammalian (Takara). The input quantity of total RNA was comprised between 1 and 22ng. This protocol includes a first step of RNA fragmentation, using a proprietary fragmentation mix at 94°C. The time of incubation was set up for each sample, based on the RNA quality, and according to the

manufacturer's recommendations. After fragmentation, indexed cDNA synthesis was performed. Then the ribodepletion step was performed, using probes specific to mammalian rRNA. PCR amplification was finally achieved to amplify the indexed cDNA libraries, with a number of cycles set up according to the input quantity of tRNA. Library quantification and quality assessment was performed using Qubit fluorometric assay (Invitrogen) with dsDNA HS (High Sensitivity) Assay Kit and LabChip GX Touch using a High Sensitivity DNA chip (Perkin Elmer). Libraries were then equimolarly pooled and quantified by qPCR using the KAPA library quantification kit (Roche). Sequencing was carried out on the NovaSeq 6000 (Illumina), targeting between 10 and 15M reads per sample and using paired-end 2 x 100 bp.

Gene set enrichment analysis

To statistically evaluate the enrichment of previously reported gene signatures and DEG calculated from pairwise comparison in this study (Gene Sets), we used pairwise comparisons using the gene set enrichment analysis (GSEA)[82] method from the Massachussets Institute of Technology (https://www.broadinstitute.org/gsea). Statistical analysis was performed by evaluation of nominal p value and false discovery rate (q value) based on 1,000 random permutations. Results were considered significant when the p value was below 0.05 and when the q value was below 0.25 (false discovery rate below 25%) accordingly to the recommendation from the software developers.

scRNA-seq analysis

For cell sorting experiments, tumor-bearing lungs and tdLN were collected and processed as previously described. The strategy used for the sort is depicted in the figures. The droplet-based approach of 10X Genomics platform was used to perform scRNA-seq. For each scRNA-seq sample, cell suspension from three individual mice were pooled and sorted in PBS containing 0,04%BSA. 10 000 cells were loaded on a Chromium Controller using the Chromium Next GEM Single Cell 3 Reagent Kits v3.1 according to manufacturer instructions.

Raw sequencing reads were processed using the 10x Genomics software Cellranger. To obtain a cell count matrix, reads were mapped to the mouse GRCm38.84 reference genome. scRNA-seq analysis was performed using Seurat v4. For each dataset, cells with low genes per cell or with a high percentage of mitochondrial genes were removed from downstream analyses. Following data QC we obtained 4421 cells from the lungs KP $CD8^+$ T cells dataset, 1404 cells for the tdLN KP WT $CD8^+$ T cells dataset, 3340 cells for the tdLN KP *CD11c*^{IRF4} $CD8^+$ T cells dataset, 2076 cells for the tdLN KP WT $CD11c^+MHCII^+$ cells dataset and 3150 cells for the tdLN KP *CD11c*^{IRF4} $CD11c^+MHCII^+$ cells dataset. RNA and ADT expression were normalized separately using the default Seurat LogNormalize and Centered Log Ratio (CLR) approaches, respectively. Top 2000 most variable genes were then determined by applying a VST (Variance Stabilizing Transformation). Datasets were analyzed separately or were integrated together before analysis. For integration, top 2000 most variable genes across datasets were used as anchors with the LogNormalize method. Dimensionality reduction was performed using PCA and the top informative principle components were determined after visualization

with an elbow plot and dimensional reduction heatmaps, and used for the non-linear dimensionality reduction technique UMAP. Louvain clustering of the data was performed across a range of resolution parameters visualized using a clustree. Cluster of cells with low number of genes and in which no T lymphocyte cell identifying genes could be detected were not considered in the analysis. Subsequent analyses were performed using Seurat default parameters.

Adoptive transfers

Mediastinal lymph nodes from donor mice (CD45.2$^+$ or CD45.1$^+$ tumor-bearing or CD45.1$^+$ OTI x Rag1$^{-/-}$ tumor-free mice) were mechanically dissociated on a 70µm cell strainers in sterile FACS buffer. After two washes in PBS, the LN cell suspensions were counted as previously described and resuspended in 100µL of RPMI without supplement and intravenously injected in recipient mice (CD45.1$^+$ or CD45.2$^+$ tumor-bearing mice), according to the experimental designs described in figures 2K, S5O, 5G and S7L.

Ex vivo Mouse T cell priming assay

OT-1 cell preparation:

OT-1 CD8$^+$ T cells were isolated from lymph nodes of CD45.1$^+$ OTI x Rag1$^{-/-}$ mice and labeled for proliferation assay with 2µM of CellTrace Violet (CTV, Invitrogen) at 37°C for 15 minutes, washed and counted before culture with DC subsets.

Dendritic cells isolation from LNs:

For the isolation of mediastinal lymph node DCs from KP- or KP-OVA bearing mice, minced mediastinal tumor-draining LNs were digested in 500µl HBSS with calcium and

magnesium (Thermo Fisher) with 75 µg/mL of Liberase TL (Roche) and 0.02mg/ml DNase I (Thermo Fisher) and incubated at 37°C for 20 minute under agitation. Cell suspensions were passed through a 70µm cell strainers. Cell suspensions were then blocked in FcBlock and stained with CD11c-biotin followed by SAV-beads (Miltenyi). Cell suspension was applied on a LS column (Miltenyi) according to the manufacturer's instructions. The CD11c-enriched fraction retained in the column was then stained for CD11c, MHCII, CD19, XCR1 and CD11b. Dendritic cells subsets were FACS-sorted on a Melody (BD) according to the gating strategy depicted on the Fig.s.

DCs and T cell co-culture:

2500 DCs were plated in V-bottom 96 well plates and incubated with 25000 CTV-loaded OT-1 in RPMI medium (10% FCS + 1% Pencillin/Streptomycin + 1mM Sodium Pyruvate 55µM 2-mercaptoethanol and 10mM HEPES). When indicated, various doses of the SIINFEKL OVA peptide or mutated peptides (Q4, T4, G4) were added to the cultures at the indicated concentration. For some experiments, recombinant mouse TGF-β (20µg/mL) (Biolegend), recombinant mouse IL-12p70 (20µg/mL) (Biolegend) or anti-IL-12p40 blocking antibody (20µg/mL) (Biolegend) were added to the well.

T cell activation analysis by flow cytometry:

After 48h or 96h of co-culture as indicated in the figures, T cells were stained for CD45.1, CD8, CD44, CD62L, PD-1 and CD103 to analyze their activation and polarization status. CTV dilution was analyzed to assess T cell proliferation.

Quantification and Statistical Analysis

Statistical analysis was performed using Prism 10 (GraphPad Software Inc., USA). Each dot displayed on the graphs corresponds to one biological replicate and error bars represent standard deviations. When two experimental groups were compared, two-tailed unpaired or paired Student's t test was used. When three or more groups were compared, statistically significant differences between means were determined using the one-way analysis of variance (ANOVA) method. Tukey's multiple comparisons test was applied when comparing multiple conditions. A p-value of less than 0.05 was considered as significant, indicated with the following signs: *$p < 0.05$, **$p < 0.01$, ***$p < 0.001$, ****$p < 0.0001$.

EXTENDED DATA

Figs. S1 to S8

Supplementary Figure 1 - T_{RM}-like CD8$^+$ T cells infiltrate lung tumors

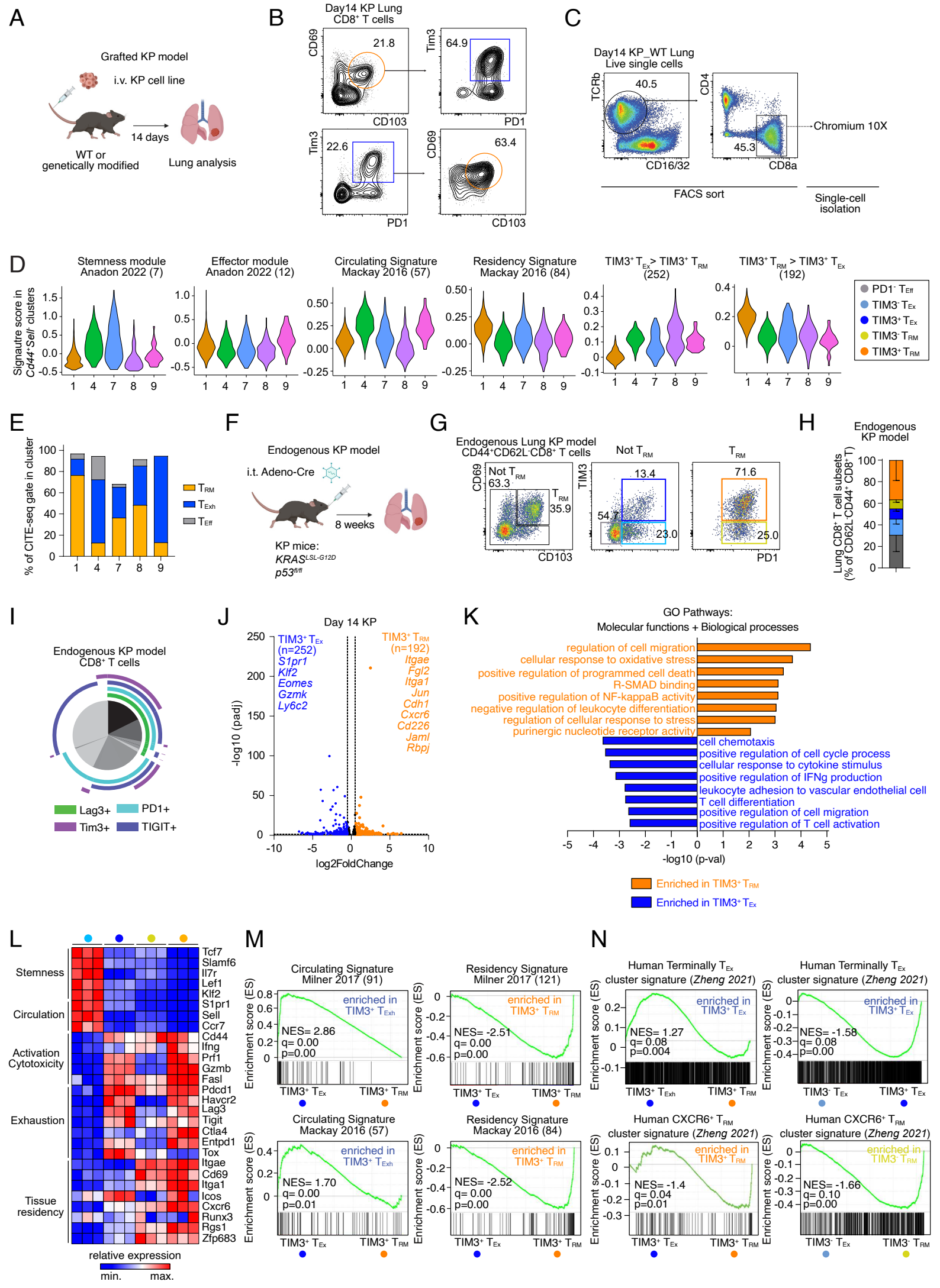

Fig. S1. T_{RM}-like $CD8^+$ T cells infiltrate lung tumors.

(**A**) Schematic for the grafted model of KP lung adenocarcinoma. WT or genetically modified mice are injected intravenously with the KP cell line and tumoral lung microenvironment is assessed at 14 days post-injection.

(**B**) Representative flow cytometry plots showing the proportion of $PD1^+TIM3^+$ cells within $CD69^+CD103^+$ $CD8^+$ T cells or, vice versa, the proportion of $CD69^+CD103^+$ cells within $PD1^+TIM3^+$ $CD8^+$ T cells in the lungs of KP tumor-bearing mice.

(**C**) $CD8^+$ T cells were sorted by flow cytometry from pooled lungs of 3 KP tumor-bearing mice before scRNA-seq analysis. Single cells were isolated using a 10X Chromium droplet-based approach and sequenced.

(**D**) Violin Plots showing the scoring of indicated gene signatures across activated scRNA-seq clusters[4,11,16].

(**E**) Distribution of CITE-Seq gated $CD44^+CD62L^-PD1^+CD69^+CD103^+$ T_{RM}, $CD44^+CD62L^-PD1^+Not(CD69^+CD103^+)$ T_{Exh} and $CD44^+CD62L^-PD1^-$ T_{Eff} across *Cd44*$^+$*Sell*$^-$ clusters

(**F**) Schematic for the endogenous lung adenocarcinoma mouse model. $KRAS^{LSL\text{-}G12D}$ *p53*$^{fl/fl}$ mice were injected intratracheally with an adenovirus coding for the Cre recombinase (Adeno-Cre)[76]. Tumoral lung microenvironment was assessed at 8-weeks post-intra-tracheal adenovirus-Cre instillation.

(**G-H**) Representative flow cytometry plots (G) and quantification (H) of lung $CD44^+CD62L^-CD8^+$ T cell populations in the endogenous KP model.

(**I**) Boolean gating strategy was used on lung $CD8^+$T cells for analysis in the endogenous KP model. Pie charts represent the frequency of cells positive for the given number of co-inhibitory markers (PD1, TIGIT, LAG3, and TIM3). Arcs depict the relative frequency of

cells specifically positive for PD1, TIGIT, LAG3 and/or TIM3 staining, as indicated (n = 8 mice).

(**J-N**) Bulk RNA-sequencing analysis of sorted $CD8^+$T cell populations as defined in Figure 1H.

(**J**) Volcano plot representing differentially expressed genes (DEGs) between $TIM3^+$ T_{RM} and $TIM3^+$ T_{Exh}. Genes with a Log2(fold change, FC) > ±2 and a false discovery rate (FDR)-adjusted p-value of less than 0.05 were considered significant.

(**K**) Differential enrichment of gene pathways (Gene ontology Molecular function and Biological processes) comparing $TIM3^+$ T_{RM} and $TIM3^+$ T_{Exh}.

(**L**) Relative expression of genes related to stemness, circulation, activation-cytotoxicity, exhaustion and tissue-residency.

(**M**) GSEA of pairwise comparisons of $TIM3^+$ T_{RM} versus $TIM3^+$ T_{Exh} using genes from residency and circulating signatures[4,11] (NES, normalized enrichment score).

(**N**) GSEA of pairwise comparisons of $TIM3^+$ T_{RM} versus $TIM3^+$ T_{Exh}, $TIM3^+$ T_{Exh} versus $TIM3^-$ T_{PExh} or $TIM3^+$ T_{RM} versus $TIM3^-$ T_{RM} using genes from human terminally exhausted and human $CXCR6^+$ T_{RM} in pan-cancer context[83](NES, normalized enrichment score).

Supplementary Figure 2 - T_{RM}-like CD8$^+$ TILs exhibit anti-tumoral properties and respond to ICB

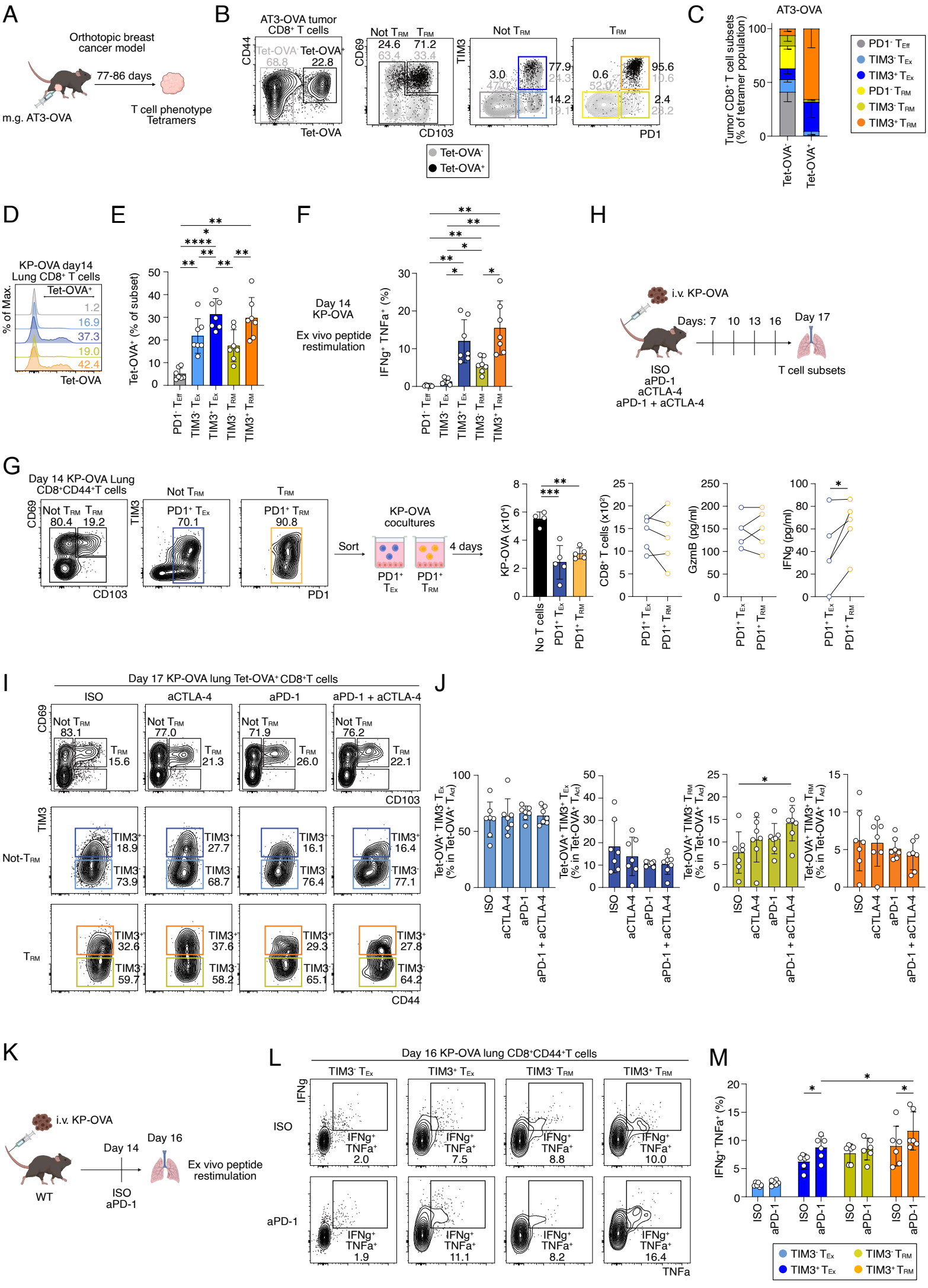

Fig. S2. T_{RM}-like $CD8^+$ TILs exhibit anti-tumoral properties and respond to ICB.

(**A**) Schematic for the orthotopic model of AT3-OVA breast cancer. C57Bl6/J mice are injected in the mammary gland with the AT3-OVA cell line and tumor-specific T cells are analyzed 77 to 86 days later when tumors reach the limit size of $1500mm^3$.

(**B**) Representative flow cytometry gating strategy showing the phenotype of tetramer-OVA^+ (dark) or tetramer-OVA^- cells (grey) infiltrating AT3-OVA breast tumors.

(**C**) Quantification of the proportions of tetramer-OVA^+ or tetramer-OVA^- $CD8^+$ T cell populations infiltrating breast AT3-OVA tumors (n = 5 mice, paired two-way anova).

(**D-E**) Representative histogram (**D**) and quantifications (**E**) of the proportions of tetramer-OVA^+ cells within $CD8^+$ TILs populations (n = 7 mice, paired one-way anova).

(**F**) $CD8^+$ TILs were isolated from the lungs of KP-OVA bearing mice at day 14 post-injection and restimulated *ex vivo* with 1µM OVA-specific SIINFEKL peptide for 5-hours. The percentage of double-positive $IFN\gamma^+TNF\alpha^+$ are quantified (n = 7 mice, paired one-way anova).

(**G**) $PD1^+$ T_{Ex} and $PD1^+$ T_{RM} were sorted from the lungs of KP-OVA bearing mice at day 14 and cocultured for 4 days with KP-OVA tumor cells. At the end of the coculture absolute numbers of KP-OVA tumor cells and $CD8^+$ T cells and concentrations of GzmB and IFNγ in the supernatant were quantified.

(**H-J**) KP-OVA tumor-bearing mice were chronically treated every 3 days starting at day 7 post-tumor inoculation with control isotype, anti-PD-1, anti-CTLA-4 or both antibodies and tetramer-OVA^+ T cell subsets were analyzed in the lungs at day 17.

(**H**) Schematic of the experiment

(**I-J**) Representative flow cytometry plots (**I**) and quantifications (**J**) of the proportions of each subset within tetramer-OVA$^+$ CD8$^+$ T cells.

(**K-L**) KP-OVA tumor-bearing mice were acutely treated with control isotype or anti-PD-1 antibodies at day 14 post-tumor inoculation and lung CD8+ TILs were isolated at day 16 and restimulated *ex vivo* with 1µM OVA-specific SIINFEKL peptide for 5-hours.

(**K**) Schematic of the experiment

(**L-M**) Representative flow cytometry plots (**L**) and quantifications (**M**) of the percentage of double-positive IFNγ$^+$TNFα$^+$within CD8$^+$ TILs populations (n = 6 mice, paired one-way anova).

Supplementary Figure 3 - Tumor-draining lymph nodes contain a fraction of CD103⁺ activated CD8⁺ T cells poised to generate T_{RM}-like TILs

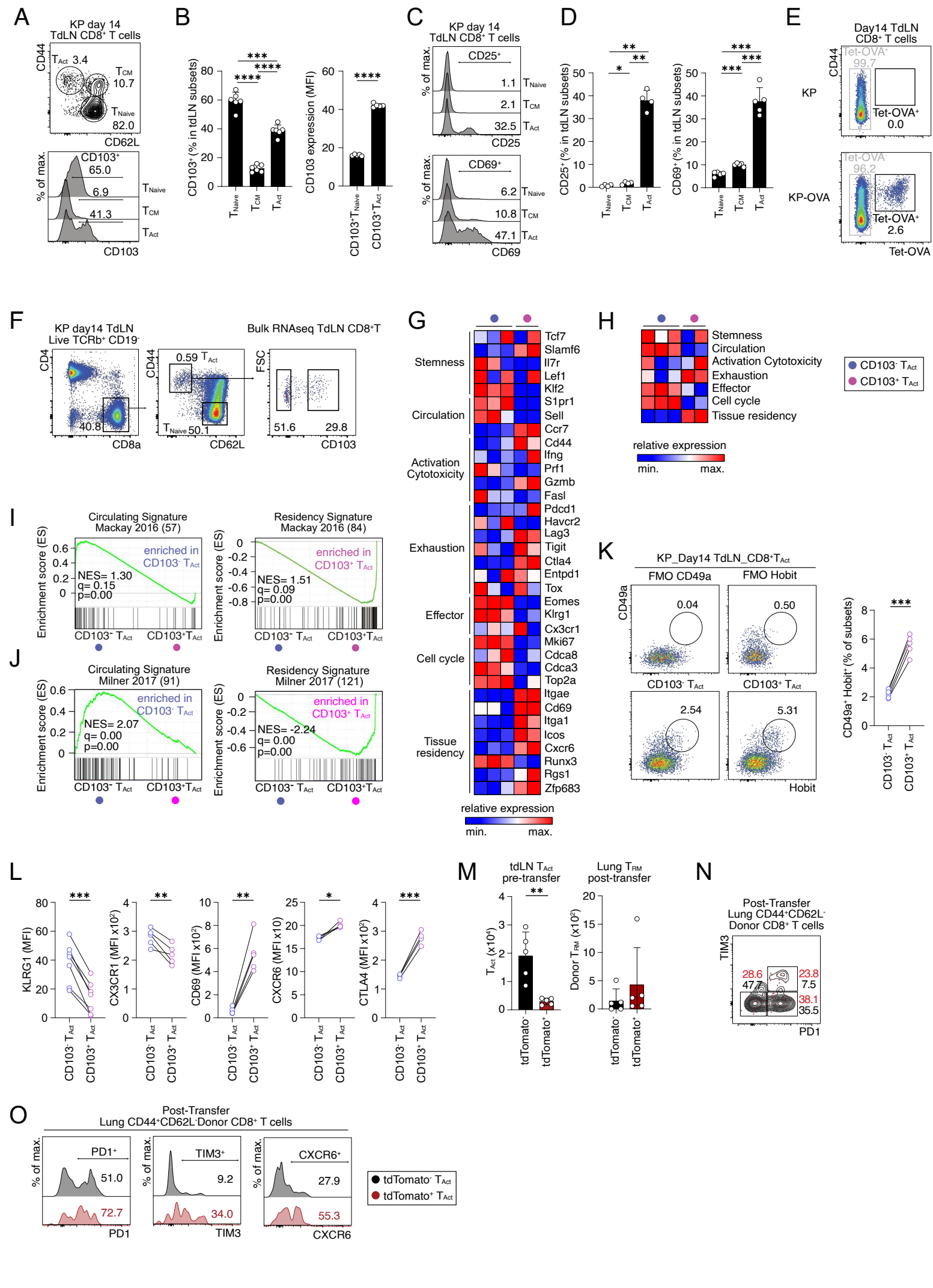

Fig. S3. Tumor-draining lymph nodes contain a fraction of CD103$^+$ activated CD8$^+$ T cells poised to generate T_{RM}-like TILs.

(**A-B**) Representative flow cytometry plot for the gating of naïve (T_{Naive}, CD44$^-$CD62L$^+$), central memory (T_{CM}, CD44$^+$CD62L$^+$) and activated (T_{Act}, CD44$^+$CD62L$^-$) CD8$^+$ T cells in KP day 14 tdLN and histogram of CD103 expression within these populations (A) and associated quantifications (B) (n = 6 KP mice, paired one-way anova (left graph) and paired t-test (right graph)).

(**C-D**) Representative flow cytometry histograms showing the expression of CD25 or CD69 within KP tdLN CD8+ T cell subsets (C) and associated quantifications (D) (n = 4 KP mice for CD25 and n = 5 KP mice for CD69, paired one-way anova).

(**E**) Representative flow cytometry plots showing the gating of tetramer-OVA$^+$ CD8$^+$ T cells in KP-OVA but not KP tdLNs.

(**F**) Gating strategy to sort KP tdLN CD103$^-$ T_{Act} and CD103$^+$ T_{Act} for bulk RNA-sequencing.

(**G-H**) Relative expression of genes related to stemness, circulation, activation-cytotoxicity, exhaustion, effector, cell cycle and tissue-residency for CD103$^+$ and CD103$^-$ T_{Act} populations (G) and global signature scoring of these modules (H).

(**I-J**) GSEA of pairwise comparisons of CD103$^+$ T_{Act} vs CD103$^-$ T_{Act} using genes from residency and circulating signatures[4,11].

(**K**) Representative flow cytometry plots and quantification of CD49a$^+$Hobit$^+$ expression in CD103$^-$ T_{Act} and CD103$^+$ T_{Act} (n = 5 KP mice, paired t-test).

(**L**) Quantifications of the median fluorescent intensity (MFI) of indicated markers within CD103$^-$ T_{Act} and CD103$^+$ T_{Act} (n = 4-7 KP mice, paired t-test).

(**M**) Quantifications of the absolute numbers of tdTomato$^-$ or tdTomato$^+$ T_{Act} in donor tdLN pre-transfer (left) or donor T_{RM}-like in recipient lungs post-transfer (right).

(**N**) Representative flow cytometry plot showing the expression of PD1 and TIM3 by tdTomato$^-$ (black) and tdTomato$^+$ (red) donor cells in recipient lungs post-transfer.

(**O**) Representative histograms showing the expression of PD1, TIM3 and CXCR6 by tdTomato$^-$ and tdTomato$^+$ donor cells in recipient lungs post-transfer.

Supplementary Figure 4 - CD103+ activated T cells in tdLN contain a tumor antigen-specific population of CXCR6+ T_{RM} precursors

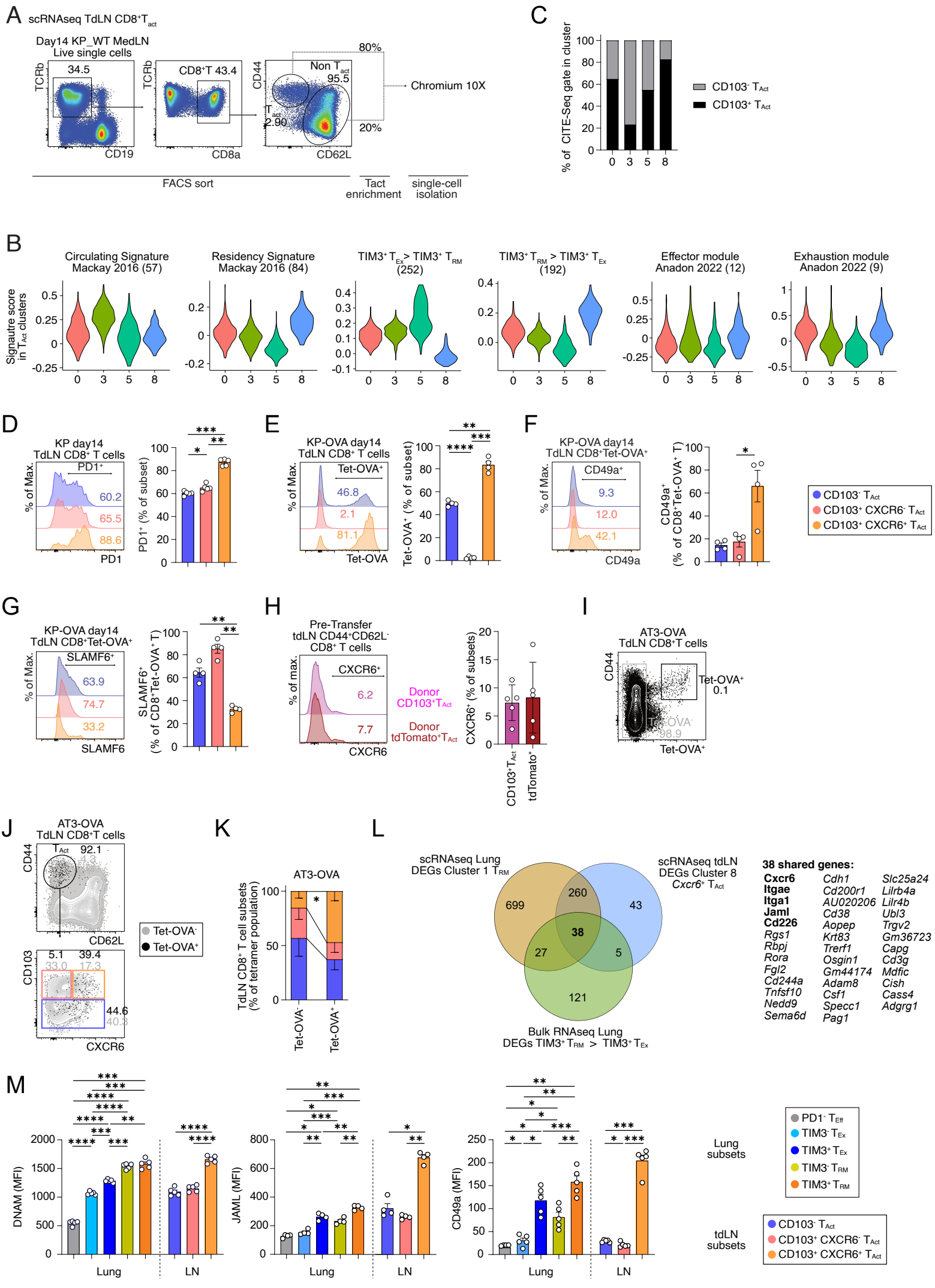

Fig. S4. CD103$^+$ activated T cells in tdLN contain a tumor antigen-specific population of CXCR6$^+$ T_{RM} precursors.

(**A**) CD8$^+$ T cell subsets were sorted by flow cytometry from pooled tdLNs of 3 KP-bearing mice before scRNA-seq analysis. To improve the resolution of CD8$^+$ T_{Act}, the cellular input was enriched in T_{Act} (80%) mixed with T_{CM} and T_{Naive} (20%). Single cells were isolated using a 10X Chromium droplet-based approach and sequenced.

(**B**) Violin Plots showing the scoring of indicated gene signatures across activated clusters[4,11,16].

(**C**) Distribution of CITE-Seq gated CD103$^-$ T_{Act} and CD103$^+$ T_{Act} across T_{Act} clusters.

(**D**) Representative flow cytometry histogram and quantification of PD1 expression across KP tdLN T_{Act} subsets (n = 5 mice, paired one-way ANOVA test).

(**E**) Representative histogram and quantifications of the proportions of tetramer-OVA$^+$ cells within KP-OVA tdLN T_{Act} subsets (n = 4 mice, paired one-way anova test).

(**F**) Representative flow cytometry histogram and quantification of CD49a$^+$ cells across KP-OVA tdLN tetramer-OVA$^+$ T_{Act} subsets (n = 4 mice, paired one-way ANOVA test).

(**G**) Representative flow cytometry histogram and quantification of SLAMF6$^+$ cells across KP-OVA tdLN tetramer-OVA$^+$ T_{Act} subsets (n = 4 mice, paired one-way ANOVA test).

(**H**) Representative flow cytometry histogram and quantification of CXCR6 expression within CD103$^+$ T_{Act} or tdTomato$^+$ T_{Act} from donor tdLN CD45.2$^+$ CD103^{ERcre} x ROSA$^{LSL\text{-}tdTomato}$ pre-transfer (see also Fig.2K).

(**I**) Representative flow cytometry plot showing the gating of tetramer-OVA$^+$ CD8$^+$ T cells in AT3-OVA tdLNs.

(**J**) Representative flow cytometry gating strategy showing the phenotype of tetramer-OVA$^+$ (dark) or tetramer-OVA$^-$ cells (grey) in AT3-OVA tdLN.

(**K**) Quantification of the proportions of tetramer-OVA$^+$ or tetramer-OVA$^-$ CD8$^+$ T cell populations in AT3-OVA tdLN (n = 5 mice, paired two-way anova test).

(**L**) Venn diagram showing the overlap between genes upregulated in lung scRNA-seq cluster C1 (orange), tdLN scRNA-seq cluster C8 (dark blue) and DEGs from TIM3$^+$ T_{RM} > TIM3$^+$ T_{Exh} (green). Shared genes (38) are written on the right of the diagram.

(**M**) Flow cytometry quantification of the expression of conserved T_{RM} marker genes DNAM, JAML and CD49a across lung and tdLN subsets as defined previously (n = 4-5 mice, paired one-way ANOVA tests).

Supplementary Figure 5 - Both XCR1⁺ and CD11b⁺ DCs contribute to the differentiation of T_{RM} precursors in tdLN

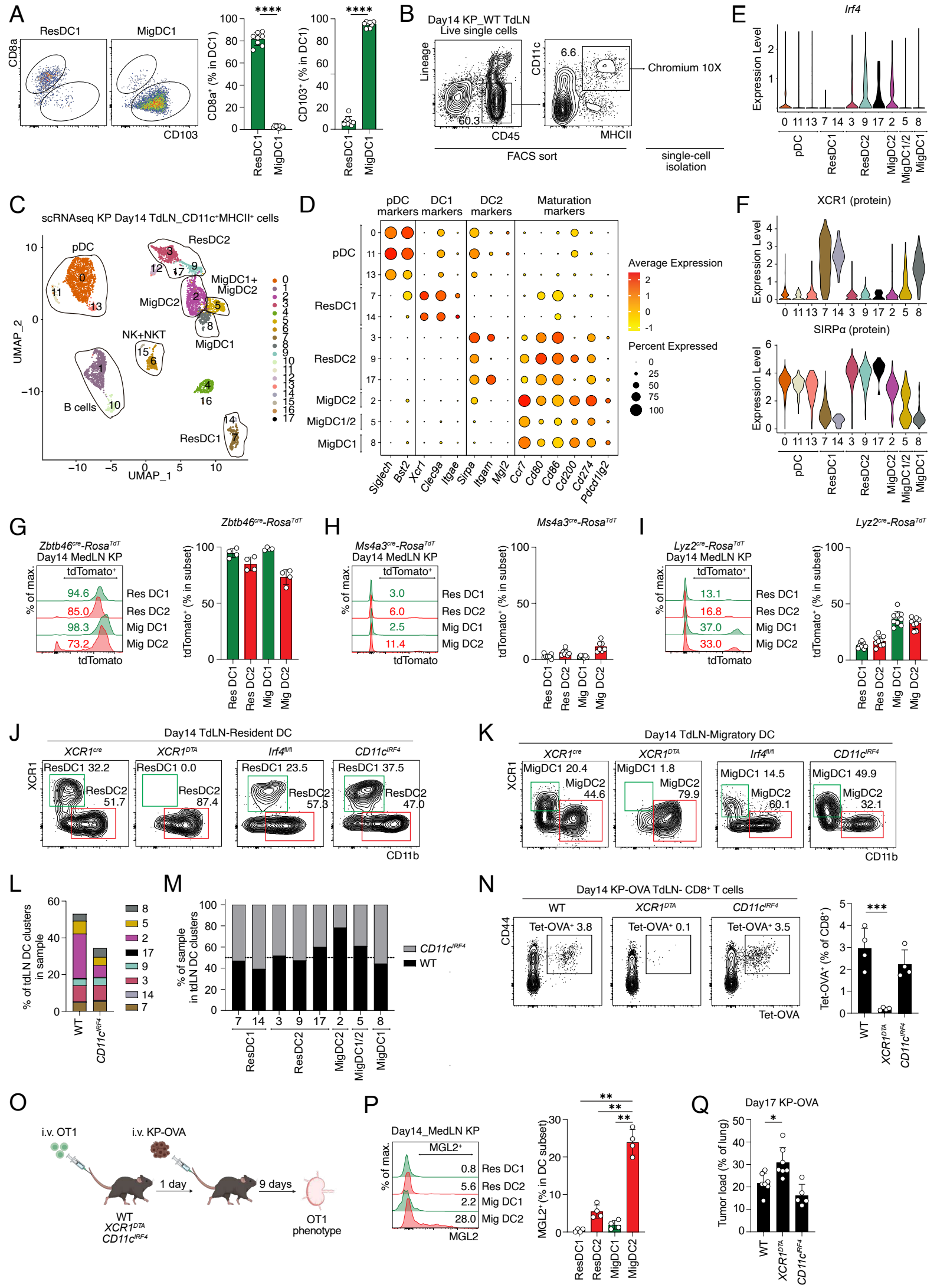

Fig. S5. Both XCR1$^+$ and CD11b$^+$ DCs contribute to the differentiation of T_{RM} precursors in tdLN.

(**A**) Representative flow cytometry plots and quantification of the expression of CD8α and CD103 by resident or migratory DC1 (n = 8 mice, paired t-tests).

(**B**) CD11c$^+$ MHCII$^+$ cells were sorted by flow cytometry from pooled tdLNs of 3 KP-bearing mice before scRNA-seq analysis. Single cells were isolated using a 10X Chromium droplet-based approach and sequenced.

(**C**) UMAP dimensionality reduction embedding the different clusters.

(**D**) Dot Plot showing the expression of core marker genes across clusters.

(**E**) Violin Plots showing the RNA expression of *Irf4* across dendritic cell clusters.

(**F**) Violin Plots showing the CITE-Seq protein expression of core DC1 (XCR1) or DC2 (SIRPα) markers across dendritic cell clusters.

(**G-I**) Representative histograms and quantifications of tdTomato expression within tdLN resident and migratory DC subsets in *Zbtb46^{cre}-Rosa$^{LSL\text{-}tdTomato}$* (G), *Ms4a3^{cre}-Rosa$^{LSL\text{-}tdTomato}$* (H) and *Lyz2^{cre}-Rosa$^{LSL\text{-}tdTomato}$* (I) mice bearing KP tumors at day 14 (n = 4 *Zbtb46^{cre}-Rosa$^{LSL\text{-}tdTomato}$*, n = 7 *Ms4a3^{cre}-Rosa$^{LSL\text{-}tdTomato}$* and n = 9 *Lyz2^{cre}-Rosa$^{LSL\text{-}tdTomato}$* mice, paired one-way anova tests).

(**J-K**) Representative flow cytometry plots of resident (J) or migratory (K) DC1 and DC2s in WT, *XCR1^{DTA}* and *CD11c^{IRF4}* mice bearing KP tumors.

(**L-M**) Proportion of each tdLN scRNAseq dendritic cell clusters in WT or *CD11c^{IRF4}* samples (L) or, vice versa, of WT or *CD11c^{IRF4}* samples in each dendritic cell cluster (M).

(**N**) Representative flow cytometry plots and quantification of tdLN tetramer-OVA$^+$ CD8$^+$ T cell populations in KP-OVA bearing WT, *XCR1*^{DTA} or *CD11c*^{IRF4} mice (n = 4 mice per group, one-way anova test).

(**O**) Experimental design for the adoptive transfer of OT1 quantified in Figure 3J. CD45.1$^+$ OT1 cells were transferred intravenously into WT, *XCR1*^{DTA} and *CD11c*^{IRF4} mice 1 day before KP-OVA tumor cells injection. 9 days later, tdLN were harvested to assess OT1 phenotype.

(**P**) Representative histogram and quantification of MGL2 protein expression within KP tdLN resident and migratory DC subsets at day 14 (n = 4 mice, one-way anova test).

(**Q**) Quantification of tumor loads in the lungs of WT, *XCR1*^{DTA} and *CD11c*^{IRF4} mice bearing KP-OVA tumors at day 17 (n = 7 WT, n = 7 *XCR1*^{DTA} and n = 5 *CD11c*^{IRF4} mice, one-way anova test).

Supplementary Figure 6 - Both XCR1⁺ and CD11b⁺ DCs contribute to the differentiation of T_{RM} precursors in AT3-OVA tdLN

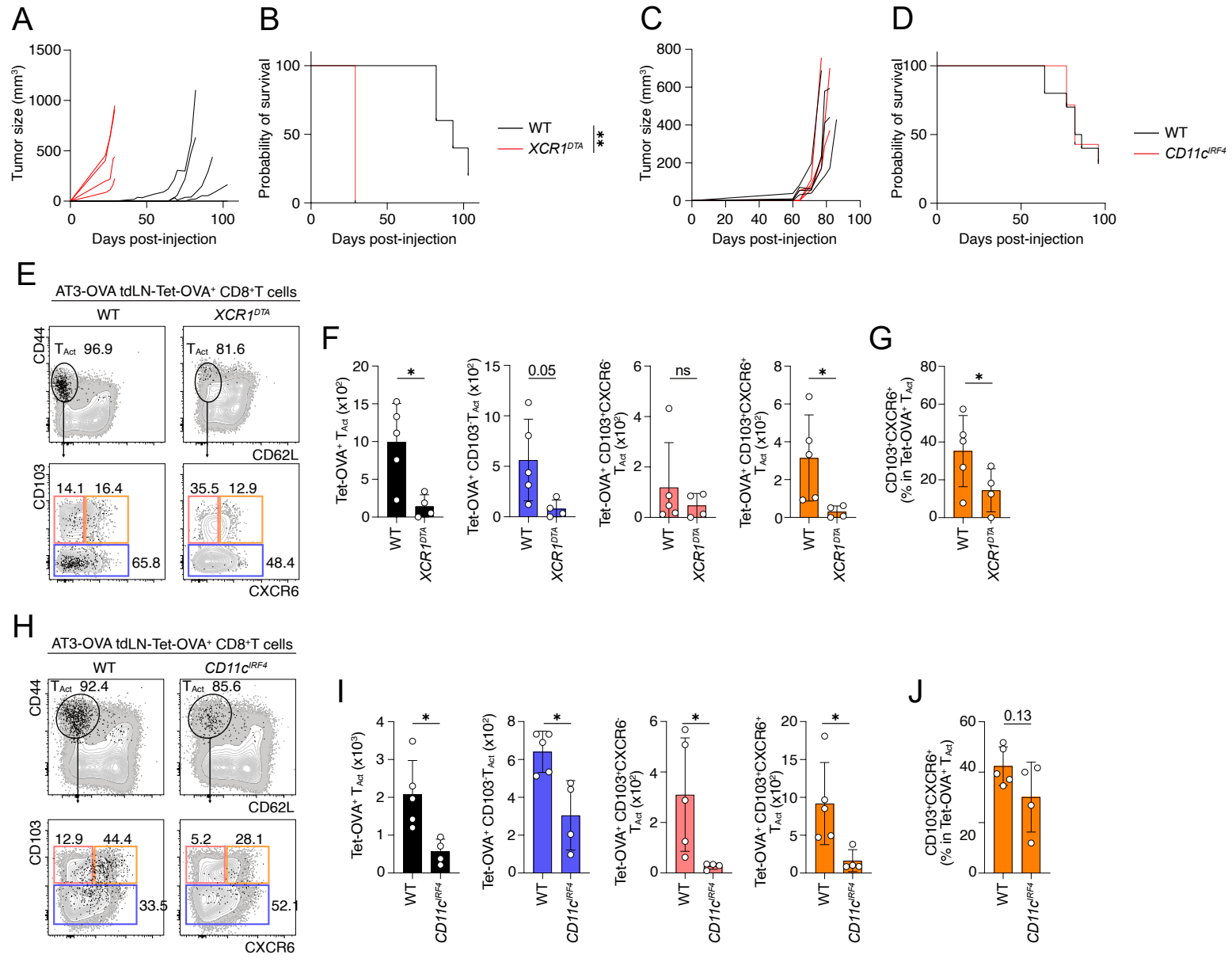

Fig. S6. Both XCR1$^+$ and CD11b$^+$ DCs contribute to the differentiation of T_{RM} precursors in AT3-OVA tdLN.

(**A-B**) Tumor growth (A) and survival curve (B) of WT or *XCR1^{DTA}* mice injected orthotopically with AT3-OVA tumors.

(**C-D**) Tumor growth (C) and survival curve (D) of WT or *CD11c^{IRF4}* mice injected orthotopically with AT3-OVA tumors.

(**E-G**) Representative flow cytometry plots (E) and quantifications of tdLN tetramer-OVA$^+$ T_{Act} subsets in absolute numbers (F) or in frequency within tetramer-OVA$^+$ T_{Act} (G) in AT3-OVA bearing WT or *XCR1*^{DTA} mice (n = 5 WT, n = 4 *XCR1*^{DTA}, unpaired t-tests). Mice were analyzed when tumors reached the limit size of 1500mm^3. Black tetramer-OVA$^+$ cells overlay grey tetramer-OVA$^-$ cells.

(**H-J**) Representative flow cytometry plots (H) and quantifications of tdLN tetramer-OVA$^+$ T_{Act} subsets in absolute numbers (I) or in frequency within tetramer-OVA$^+$ T_{Act} (J) (n = 5 WT, n = 4 *CD11c*^{IRF4}, unpaired t-tests). Mice were analyzed when tumors reached the limit size of 1500mm^3. Black tetramer-OVA$^+$ cells overlay grey tetramer-OVA$^-$ cells.

Supplementary Figure 7 - Efficient generation of T_{RM}-like TILs requires both DC1s and DC2s at the level of tdLN

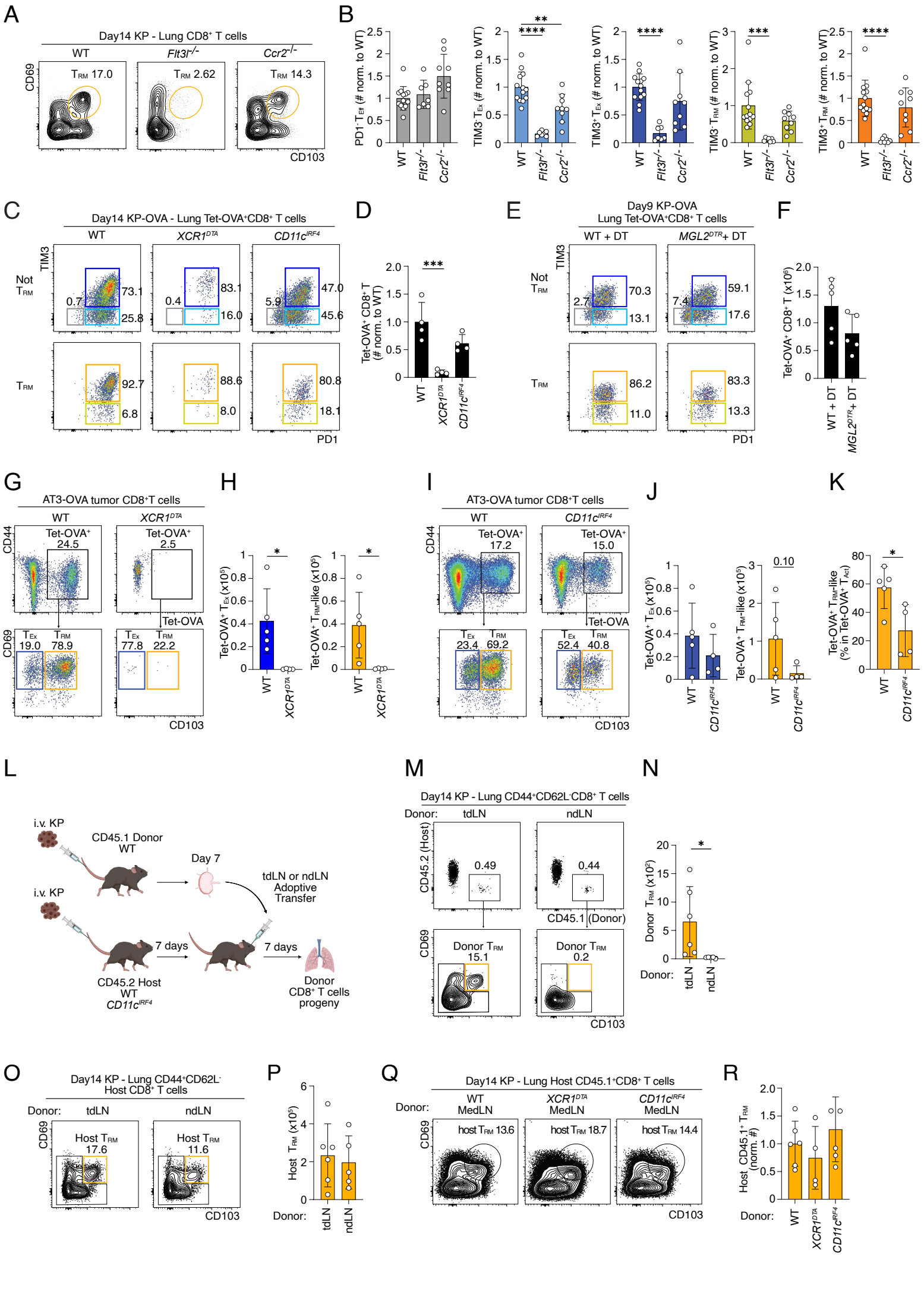

Fig. S7. Efficient generation of T_{RM}-like TILs requires both DC1s and DC2s at the level of tdLN.

(**A-B**) Representative flow cytometry plots (A) and quantifications (B) of lung CD8$^+$ T cell subsets in WT, *Flt3l*$^{-/-}$ or *Ccr2*$^{-/-}$mice bearing KP-tumors (n = 11 WT, n = 7 *Ftl3l*$^{-/-}$ and n = 8 *Ccr2*$^{-/-}$ mice, one-way ANOVA tests).

(**C**) Representative flow cytometry plots of lung tetramer-OVA$^+$ CD8$^+$ T cell populations in KP-OVA bearing WT, *XCR1*^{DTA} or *CD11c*^{IRF4} mice.

(**D**) Quantification of lung total tetramer-OVA$^+$ CD8$^+$ T cells in WT, *XCR1*^{DTA} or *CD11c*^{IRF4} mice bearing KP-OVA tumors (n = 4 mice per group, one-way ANOVA tests).

(**E**) Representative flow cytometry plots of lung tetramer-OVA$^+$ CD8$^+$ T cell populations in KP-OVA bearing WT or *Mgl2*^{DTR} mice treated with diphteria toxin.

(**F**) Quantification of lung total tetramer-OVA$^+$ CD8$^+$ T cells in WT or *Mgl2*^{DTR} mice treated with diphteria toxin bearing KP-OVA tumors (n = 5 mice per group, one-way ANOVA tests).

(**G-H**) Representative flow cytometry plots (G) and quantifications of tumor tetramer-OVA$^+$ T_{Act} subsets (H) in AT3-OVA bearing WT or *XCR1*^{DTA} mice (n = 5 WT, n = 4 *XCR1*^{DTA}, unpaired t-tests). Mice were analyzed when tumors reached the limit size of 1500mm^3.

(**I-J**) Representative flow cytometry plots (I) and quantifications of tumor tetramer-OVA$^+$ T_{Act} subsets (J) in AT3-OVA bearing WT or *CD11c*^{IRF4} mice (n = 5 WT, n = 4 *CD11c*^{IRF4} mice, unpaired t-tests). Mice were analyzed when tumors reached the limit size of 1500mm^3.

(**L**) Experimental design for the adoptive transfer of LNs. Donor CD45.1$^+$ mice and host CD45.2$^+$ mice were injected with KP cells. 7 days later, total donor draining mediastinal

lymph node (tdLN) or non-draining inguinal lymph node (ndLN) were transferred intravenously in host mice. Lungs from host mice were analyzed 7 days post-transfer. (**M-N**) Representative flow cytometry plots (M) and quantifications (N) of donor CD45.1$^+$ CD8$^+$T cell populations 7 days post-transfer of tdLN or ndLN (n = 6 tdLN and n = 5 ndLN donors, unpaired t-tests).

(**O-P**) Representative flow cytometry plots (O) and quantifications (P) of host CD45.2$^+$ CD8$^+$T cell populations 7 days post-transfer of tdLN or ndLN (n = 6 tdLN and n = 5 ndLN donors, unpaired t-tests).

(**Q-R**) Representative flow cytometry plots (Q) and quantifications (R) of host CD45.1$^+$ CD8$^+$T cell populations 7 days post-transfer of WT, *XCR1*^{DTA} or *CD11c*^{IRF4} tdLN (n = 6 WT, n = 4 *XCR1*^{DTA} and n = 6 *CD11c*^{IRF4} donor mice, one-way ANOVA tests).

Supplementary Figure 8 - Low TCR triggering by migratory crosspriming DC2s favors CD103 expression while migratory DC1-derived IL-12 supports CXCR6 expression

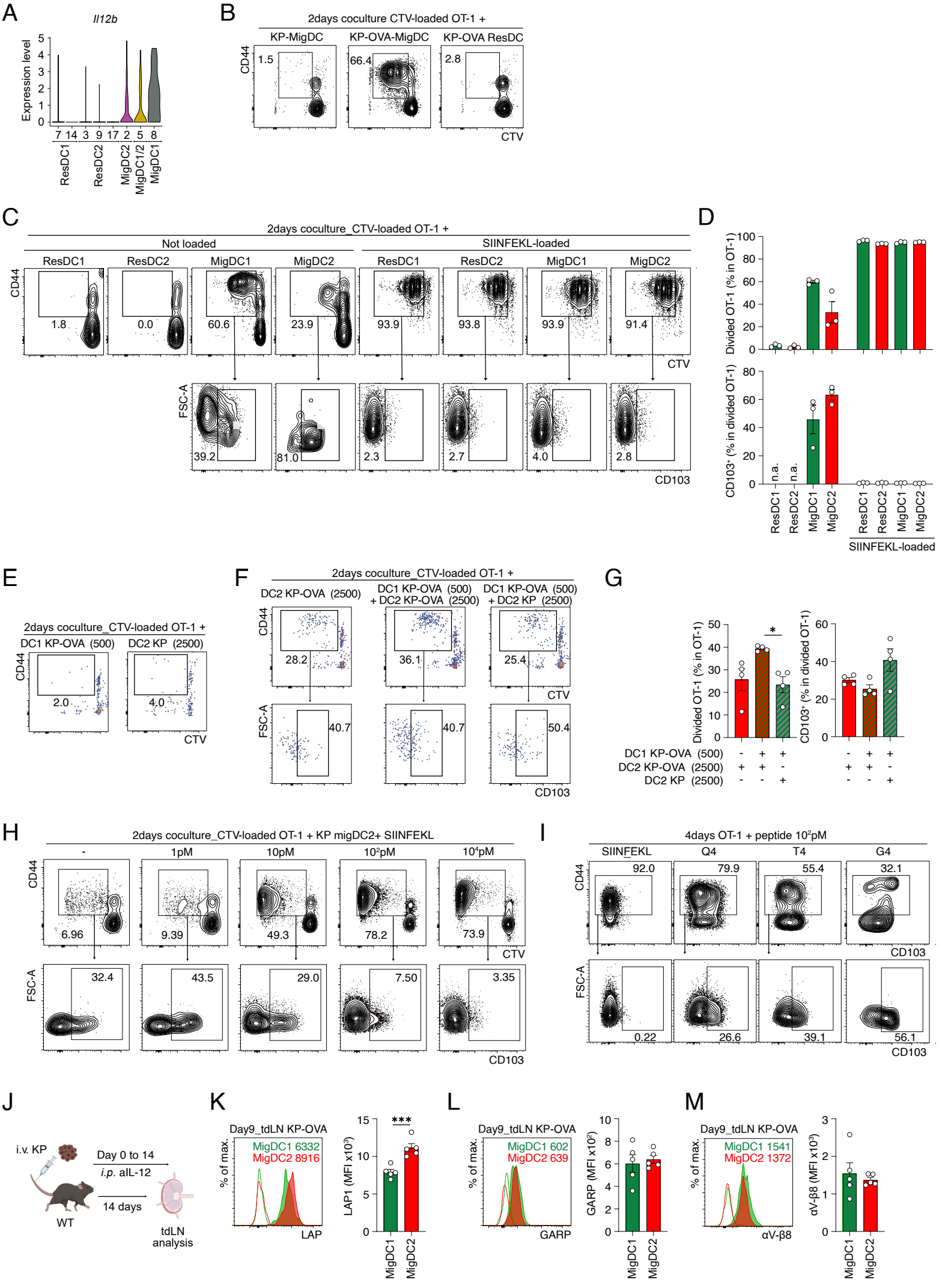

Fig. S8. Low TCR triggering by migratory crosspriming DC2s favors CD103 expression while migratory DC1-derived IL-12 supports CXCR6 expression.

(**A**) Violin plot showing the RNA expression of *Il12b* across tdLN scRNAseq dendritic cell clusters.

(**B**) Representative flow cytometry plots of CTV-loaded naïve OT-1 cells cultured for 2 days with flow cytometry-sorted migratory DCs from tdLN of mice bearing KP-tumors or migratory and resident DC from tdLN of mice bearing KP-OVA tumors.

(**C-D**) Representative flow cytometry plots (C) and quantifications (D) of CTV-loaded naïve OT-1 cells cultured for 2 days with flow cytometry-sorted resident or migratory DC1 or DC2 from tdLN of mice bearing KP tumors loaded or not with SIINFEKL peptide (n = 3 mice).

(**E**) Representative flow cytometry plots of CTV-loaded naïve OT-1 cells cultured for 2 days with flow cytometry-sorted 500 migratory cDC1 from KP-OVA tdLN or 2500 migratory DC2 from KP tdLN.

(**F-G**) Representative flow cytometry plots (F) and quantifications (G) of CTV-loaded naïve OT-1 cells cultured for 2 days with indicated combinations of flow cytometry-sorted migratory DC1 or migratory DC2 from tdLN of mice bearing KP or KP-OVA tumors (n = 4 mice per condition, paired one-way anova tests).

(**H**) Representative flow cytometry plots of OT-1 cells cultured for 2 days with flow cytometry-sorted migratory DC2 from tdLN of mice bearing KP tumors in presence of increasing SIINFEKL peptide concentration (1pM, 10pM, 10^2pM and 10^4pM) (n = 4 mice, paired one-way anova tests). See also Figure 6I.

(**I**) Representative flow cytometry plots of OT-1 cells cultured for 4 days with SIINFEKL peptide and low affinity peptides SIIQFEKL (Q4), SIITFEKL (T4) and SIIGFEKL (G4) at 10^2pM. See also Figure 6J.

(**J**) Experimental design for the *in vivo* IL-12 blockade. Mice were injected i.v. with KP tumors and treated with anti-IL-12p40 neutralizing antibody every 3 days from day 0 to 14.

(**K-M**) Representative flow cytometry plots and quantifications of LAP (K), GARP (L) and αV-β8 (M) expression by migratory DC1 and DC2 in tdLN of mice bearing KP tumors (n = 5 mice, paired t-tests). Dotted lines represent corresponding FMOs.

REFERENCES

1. Guo, X. *et al.* Global characterization of T cells in non-small-cell lung cancer by single-cell sequencing. *Nat Med* **24**, 978–985 (2018).
2. Siddiqui, I. *et al.* Intratumoral Tcf1+PD-1+CD8+ T Cells with Stem-like Properties Promote Tumor Control in Response to Vaccination and Checkpoint Blockade Immunotherapy. *Immunity* **50**, 195-211.e10 (2019).
3. Corgnac, S. *et al.* CD103+CD8+ TRM Cells Accumulate in Tumors of Anti-PD-1-Responder Lung Cancer Patients and Are Tumor-Reactive Lymphocytes Enriched with Tc17. *Cell Rep Med* **1**, 100127 (2020).
4. Milner, J. J. *et al.* Runx3 programs CD8+ T cell residency in non-lymphoid tissues and tumours. *Nature* **552**, 253–257 (2017).
5. Djenidi, F. *et al.* CD8+CD103+ tumor-infiltrating lymphocytes are tumor-specific tissue-resident memory T cells and a prognostic factor for survival in lung cancer patients. *J Immunol* **194**, 3475–3486 (2015).
6. Hombrink, P. *et al.* Programs for the persistence, vigilance and control of human CD8+ lung-resident memory T cells. *Nat Immunol* **17**, 1467–1478 (2016).
7. Ganesan, A.-P. *et al.* Tissue-resident memory features are linked to the magnitude of cytotoxic T cell responses in human lung cancer. *Nat Immunol* **18**, 940–950 (2017).
8. Savas, P. *et al.* Single-cell profiling of breast cancer T cells reveals a tissue-resident memory subset associated with improved prognosis. *Nat Med* **24**, 986–993 (2018).
9. Clarke, J. *et al.* Single-cell transcriptomic analysis of tissue-resident memory T cells in human lung cancer. *Journal of Experimental Medicine* **216**, 2128–2149 (2019).
10. Gebhardt, T. *et al.* Memory T cells in nonlymphoid tissue that provide enhanced local immunity during infection with herpes simplex virus. *Nat Immunol* **10**, 524–530 (2009).
11. Mackay, L. K. *et al.* Hobit and Blimp1 instruct a universal transcriptional program of tissue residency in lymphocytes. *Science* **352**, 459–463 (2016).
12. Fonseca, R. *et al.* Runx3 drives a CD8+ T cell tissue residency program that is absent in CD4+ T cells. *Nat Immunol* **23**, 1236–1245 (2022).
13. Skon, C. N. *et al.* Transcriptional downregulation of S1pr1 is required for the establishment of resident memory CD8+ T cells. *Nat Immunol* **14**, 1285–1293 (2013).

14. Shiow, L. R. *et al.* CD69 acts downstream of interferon-alpha/beta to inhibit S1P1 and lymphocyte egress from lymphoid organs. *Nature* **440**, 540–544 (2006).
15. Gavil, N. V. *et al.* Chronic antigen in solid tumors drives a distinct program of T cell residence. *Sci Immunol* **8**, eadd5976 (2023).
16. Anadon, C. M. *et al.* Ovarian cancer immunogenicity is governed by a narrow subset of progenitor tissue-resident memory T cells. *Cancer Cell* **40**, 545-557.e13 (2022).
17. Park, S. L. *et al.* Tissue-resident memory CD8+ T cells promote melanoma-immune equilibrium in skin. *Nature* **565**, 366–371 (2019).
18. Behr, F. M. *et al.* Tissue-resident memory CD8+ T cells shape local and systemic secondary T cell responses. *Nat Immunol* **21**, 1070–1081 (2020).
19. Low, J. S. *et al.* Tissue-resident memory T cell reactivation by diverse antigen-presenting cells imparts distinct functional responses. *J Exp Med* **217**, (2020).
20. Virassamy, B. *et al.* Intratumoral CD8+ T cells with a tissue-resident memory phenotype mediate local immunity and immune checkpoint responses in breast cancer. *Cancer Cell* **41**, 585-601.e8 (2023).
21. Nizard, M. *et al.* Induction of resident memory T cells enhances the efficacy of cancer vaccine. *Nat Commun* **8**, 15221 (2017).
22. Huang, Q. *et al.* The primordial differentiation of tumor-specific memory CD8+ T cells as bona fide responders to PD-1/PD-L1 blockade in draining lymph nodes. *Cell* **185**, 4049-4066.e25 (2022).
23. Prokhnevska, N. *et al.* CD8+ T cell activation in cancer comprises an initial activation phase in lymph nodes followed by effector differentiation within the tumor. *Immunity* **56**, 107-124.e5 (2023).
24. Mani, V. *et al.* Migratory DCs activate TGF-β to precondition naïve CD8+ T cells for tissue-resident memory fate. *Science* **366**, (2019).
25. Mackay, L. K. *et al.* The developmental pathway for CD103 + CD8 + tissue-resident memory T cells of skin. *Nature Immunology* **14**, 1294–1301 (2013).
26. Kok, L. *et al.* A committed tissue-resident memory T cell precursor within the circulating CD8+ effector T cell pool. *J Exp Med* **217**, (2020).

27. Shin, H., Kumamoto, Y., Gopinath, S. & Iwasaki, A. CD301b+ dendritic cells stimulate tissue-resident memory CD8+ T cells to protect against genital HSV-2. *Nat Commun* **7**, 13346 (2016).
28. Slütter, B. *et al.* Dynamics of influenza-induced lung-resident memory T cells underlie waning heterosubtypic immunity. *Sci Immunol* **2**, eaag2031 (2017).
29. Hildner, K. *et al.* Batf3 deficiency reveals a critical role for CD8alpha+ dendritic cells in cytotoxic T cell immunity. *Science* **322**, 1097–1100 (2008).
30. Zelenay, S. *et al.* Cyclooxygenase-Dependent Tumor Growth through Evasion of Immunity. *Cell* **162**, 1257–1270 (2015).
31. López, L. *et al.* Dendritic cell-targeted therapy expands CD8 T cell responses to bona-fide neoantigens in lung tumors. *Nat Commun* **15**, 2280 (2024).
32. Schenkel, J. M. *et al.* Conventional type I dendritic cells maintain a reservoir of proliferative tumor-antigen specific TCF-1+ CD8+ T cells in tumor-draining lymph nodes. *Immunity* **54**, 2338-2353.e6 (2021).
33. Gutiérrez-Martínez, E. *et al.* Cross-Presentation of Cell-Associated Antigens by MHC Class I in Dendritic Cell Subsets. *Front Immunol* **6**, 363 (2015).
34. Theisen, D. J. *et al.* WDFY4 is required for cross-presentation in response to viral and tumor antigens. *Science* **362**, 694–699 (2018).
35. Caronni, N. *et al.* TIM4 expression by dendritic cells mediates uptake of tumor-associated antigens and anti-tumor responses. *Nat Commun* **12**, 2237 (2021).
36. Ferris, S. T. *et al.* cDC1 prime and are licensed by CD4+ T cells to induce anti-tumour immunity. *Nature* **584**, 624–629 (2020).
37. Iborra, S. *et al.* Optimal Generation of Tissue-Resident but Not Circulating Memory T Cells during Viral Infection Requires Crosspriming by DNGR-1+ Dendritic Cells. *Immunity* **45**, 847–860 (2016).
38. Ainsua-Enrich, E. *et al.* IRF4-dependent dendritic cells regulate CD8 + T-cell differentiation and memory responses in influenza infection. *Mucosal Immunology* **12**, 1025–1037 (2019).
39. Yu, C. I. *et al.* Human CD1c+ dendritic cells drive the differentiation of CD103+ CD8+ mucosal effector T cells via the cytokine TGF-beta. *Immunity* **38**, 818–30 (2013).

40. Bourdely, P. *et al.* Transcriptional and Functional Analysis of CD1c+ Human Dendritic Cells Identifies a CD163+ Subset Priming CD8+CD103+ T Cells. *Immunity* **53**, 335-352.e8 (2020).
41. DuPage, M. *et al.* Endogenous T cell responses to antigens expressed in lung adenocarcinomas delay malignant tumor progression. *Cancer Cell* **19**, 72–85 (2011).
42. DuPage, M., Mazumdar, C., Schmidt, L. M., Cheung, A. F. & Jacks, T. Expression of tumour-specific antigens underlies cancer immunoediting. *Nature* **482**, 405–409 (2012).
43. Masopust, D. *et al.* Guidelines for T cell nomenclature. *Nat Rev Immunol* https://doi.org/10.1038/s41577-025-01238-2 (2025) doi:10.1038/s41577-025-01238-2.
44. Gueguen, P. *et al.* Contribution of resident and circulating precursors to tumor-infiltrating CD8(+) T cell populations in lung cancer. *Sci Immunol* **6**, (2021).
45. Fung, H. Y., Teryek, M., Lemenze, A. D. & Bergsbaken, T. CD103 fate mapping reveals intestinal CD103− tissue-resident memory T cells are the primary responders to secondary infection. *Sci Immunol* **7**, eabl9925 (2022).
46. Li, C. *et al.* Integrin CD103 expression in naive CD8+ T cells promotes cytokine-driven acquisition of memory phenotype and effector function. *Immunity* **58**, 2734-2752.e9 (2025).
47. Maier, B. *et al.* A conserved dendritic-cell regulatory program limits antitumour immunity. *Nature* **580**, 257–262 (2020).
48. Meredith, M. M. *et al.* Expression of the zinc finger transcription factor zDC (Zbtb46, Btbd4) defines the classical dendritic cell lineage. *J Exp Med* **209**, 1153–65 (2012).
49. Liu, Z. *et al.* Dendritic cell type 3 arises from Ly6C+ monocyte-dendritic cell progenitors. *Immunity* **56**, 1761-1777.e6 (2023).
50. Minutti, C. M. *et al.* Distinct ontogenetic lineages dictate cDC2 heterogeneity. *Nat Immunol* **25**, 448–461 (2024).
51. Mattiuz, R. *et al.* Novel Cre-Expressing Mouse Strains Permitting to Selectively Track and Edit Type 1 Conventional Dendritic Cells Facilitate Disentangling Their Complexity in vivo. *Front Immunol* **9**, 2805 (2018).

52. Bajana, S., Turner, S., Paul, J., Ainsua-Enrich, E. & Kovats, S. IRF4 and IRF8 Act in CD11c+ Cells To Regulate Terminal Differentiation of Lung Tissue Dendritic Cells. *J Immunol* **196**, 1666–77 (2016).
53. Böttcher, J. P. *et al.* NK Cells Stimulate Recruitment of cDC1 into the Tumor Microenvironment Promoting Cancer Immune Control. *Cell* **172**, 1022-1037.e14 (2018).
54. Ghislat, G. *et al.* NF-κB–dependent IRF1 activation programs cDC1 dendritic cells to drive antitumor immunity. *Sci. Immunol.* **6**, eabg3570 (2021).
55. Kumamoto, Y. *et al.* CD301b+ Dermal Dendritic Cells Drive T Helper 2 Cell-Mediated Immunity. *Immunity* **39**, 733–743 (2013).
56. Laidlaw, B. J. *et al.* CD4+ T cell help guides formation of CD103+ lung-resident memory CD8+ T cells during influenza viral infection. *Immunity* **41**, 633–645 (2014).
57. Zehn, D., Lee, S. Y. & Bevan, M. J. Complete but curtailed T-cell response to very low-affinity antigen. *Nature* **458**, 211–214 (2009).
58. Mackay, L. K. *et al.* T-box Transcription Factors Combine with the Cytokines TGF-β and IL-15 to Control Tissue-Resident Memory T Cell Fate. *Immunity* **43**, 1101–1111 (2015).
59. Luckey, C. J. *et al.* Memory T and memory B cells share a transcriptional program of self-renewal with long-term hematopoietic stem cells. *Proc Natl Acad Sci U S A* **103**, 3304–3309 (2006).
60. Diamant, I., Clarke, D. J. B., Evangelista, J. E., Lingam, N. & Ma'ayan, A. Harmonizome 3.0: integrated knowledge about genes and proteins from diverse multi-omics resources. *Nucleic Acids Research* gkae1080 (2024) doi:10.1093/nar/gkae1080.
61. Liberzon, A. *et al.* The Molecular Signatures Database Hallmark Gene Set Collection. *Cell Systems* **1**, 417–425 (2015).
62. Maru, S., Jin, G., Schell, T. D. & Lukacher, A. E. TCR stimulation strength is inversely associated with establishment of functional brain-resident memory CD8 T cells during persistent viral infection. *PLoS Pathog* **13**, e1006318 (2017).
63. Fiege, J. K. *et al.* The Impact of TCR Signal Strength on Resident Memory T Cell Formation during Influenza Virus Infection. *J Immunol* **203**, 936–945 (2019).

64. Shakiba, M. *et al.* TCR signal strength defines distinct mechanisms of T cell dysfunction and cancer evasion. *J Exp Med* **219**, e20201966 (2022).
65. Solouki, S. *et al.* TCR Signal Strength and Antigen Affinity Regulate CD8+ Memory T Cells. *J Immunol* **205**, 1217–1227 (2020).
66. Kim, T. S., Gorski, S. A., Hahn, S., Murphy, K. M. & Braciale, T. J. Distinct dendritic cell subsets dictate the fate decision between effector and memory CD8(+) T cell differentiation by a CD24-dependent mechanism. *Immunity* **40**, 400–13 (2014).
67. Slütter, B., Pewe, L. L., Kaech, S. M. & Harty, J. T. Lung airway-surveilling CXCR3(hi) memory CD8(+) T cells are critical for protection against influenza A virus. *Immunity* **39**, 939–948 (2013).
68. Bergsbaken, T., Bevan, M. J. & Fink, P. J. Local Inflammatory Cues Regulate Differentiation and Persistence of CD8+ Tissue-Resident Memory T Cells. *Cell Rep* **19**, 114–124 (2017).
69. Fung, H. Y., Espinal, A. M., Teryek, M., Lemenze, A. D. & Bergsbaken, T. STAT4 increases the phenotypic and functional heterogeneity of intestinal tissue-resident memory T cells. *Mucosal Immunol* **16**, 250–263 (2023).
70. Mami-Chouaib, F. *et al.* Resident memory T cells, critical components in tumor immunology. *J Immunother Cancer* **6**, 87 (2018).
71. Regev, O. *et al.* ICAM-1 on Breast Cancer Cells Suppresses Lung Metastasis but Is Dispensable for Tumor Growth and Killing by Cytotoxic T Cells. *Front Immunol* **13**, 849701 (2022).
72. Voehringer, D., Liang, H.-E. & Locksley, R. M. Homeostasis and effector function of lymphopenia-induced 'memory-like' T cells in constitutively T cell-depleted mice. *J Immunol* **180**, 4742–4753 (2008).
73. Caton, M. L., Smith-Raska, M. R. & Reizis, B. Notch-RBP-J signaling controls the homeostasis of CD8- dendritic cells in the spleen. *J Exp Med* **204**, 1653–1664 (2007).
74. Klein, U. *et al.* Transcription factor IRF4 controls plasma cell differentiation and class-switch recombination. *Nat Immunol* **7**, 773–782 (2006).
75. Boring, L. *et al.* Impaired monocyte migration and reduced type 1 (Th1) cytokine responses in C-C chemokine receptor 2 knockout mice. *J Clin Invest* **100**, 2552–2561 (1997).

76. DuPage, M., Dooley, A. L. & Jacks, T. Conditional mouse lung cancer models using adenoviral or lentiviral delivery of Cre recombinase. *Nat Protoc* **4**, 1064–72 (2009).
77. Reinhardt, R. L., Hong, S., Kang, S.-J., Wang, Z. & Locksley, R. M. Visualization of IL-12/23p40 In Vivo Reveals Immunostimulatory Dendritic Cell Migrants that Promote Th1 Differentiation1. *The Journal of Immunology* **177**, 1618–1627 (2006).
78. Liu, Z. *et al.* Fate Mapping via Ms4a3-Expression History Traces Monocyte-Derived Cells. *Cell* **178**, 1509-1525.e19 (2019).
79. Clausen, B. E., Burkhardt, C., Reith, W., Renkawitz, R. & Förster, I. Conditional gene targeting in macrophages and granulocytes using LysMcre mice. *Transgenic Res* **8**, 265–277 (1999).
80. Dimitrova, N. *et al.* Stromal expression of miR-143/145 promotes neoangiogenesis in lung cancer development. *Cancer Discov* **6**, 188–201 (2016).
81. Simoncello, F. *et al.* CXCL5-mediated accumulation of mature neutrophils in lung cancer tissues impairs the differentiation program of anticancer CD8 T cells and limits the efficacy of checkpoint inhibitors. *Oncoimmunology* **11**, 2059876 (2022).
82. Subramanian, A. *et al.* Gene set enrichment analysis: a knowledge-based approach for interpreting genome-wide expression profiles. *Proc Natl Acad Sci U S A* **102**, 15545–15550 (2005).
83. Zheng, L. *et al.* Pan-cancer single-cell landscape of tumor-infiltrating T cells. *Science* **374**, abe6474 (2021).

Acknowledgments

We thank M. Pittet for providing IL-12^{YFP} mice. We thank the flow cytometry and the animal facility platforms from Centre de Recherche sur l'Inflammation (CRI), Faculté de Médecine Bichat and from Institut Pasteur. We thank the NGS platforms from Institut Curie U932 and from Institut Cochin. We thank Institut National de la Santé et de la Recherche Médicale U1149 and U1016 units, Centre National de la Recherche UMR3738

unit, Institut Pasteur.

Funding

Centre National de la Recherche Scientifique CNRS (PG)

PhD Fellowship from Université de Paris (NV)

PhD Fellowship from Fondation pour la Recherche Médicale (NV)

Postdoctoral fellowship from Fondation pour la Recherche sur le Cancer ARC (PB)

Cancer Research UK

Institut National du Cancer INCA (PL-BIO22-147)

Fondation pour la Recherche sur le Cancer ARC (PJA2021060003913)

Fondation pour la Recherche Médicale (EQU202203014687)

Fondation Chercher Trouver

Fondation BMS for Immunooncology

Author contributions

Conceptualization: NV, PB, PG

Methodology: NV, PB, PG

Investigation: NV, PB, MS, AO, LG, AC, MR, AS, RS, YG, FLRDC, MV, AR, JB, AA, MG, JW, SB, KP, ZG, PhB

Software: NV, AA, SB, YG

Ressources: FG, CB, YK, GDJ, ELG, MD, TB, KVG, KH, MM, LS, JH, FB, PG

Funding acquisition: ET, JH, PG

Supervision: LS, JH, FB, PG

Writing: NV, PB, PG

Ethics declarations

Competing interests: Authors declare that they have no competing interests.

Data availability

Bulk and single-cell RNA-Seq datasets are accessible here: https://figshare.com/s/6a9c76588d496aaaa768. All original data are available from the corresponding author upon request.